NTNU – Trondheim
Norwegian University of
Science and Technology

Viscous Flow Around Finite Lenght Circular Cylinder

Pål Levold

Marine Technology
Submission date: June 2012
Supervisor: Bjørnar Pettersen, IMT

Norwegian University of Science and Technology
Department of Marine Technology

Summary

Viscous flow around circular cylinders is a classical research topic in fluid dynamics with a vast amount of practical applications in the field of offshore marine technology. In the flow around cylinders of finite length, complex wake behaviours and coherent structures occur even at relatively low Reynolds numbers. An understanding of the nature and dynamics behind such behaviour could form a basis for improved designs and innovative solutions for offshore and subsea constructions.

In the present study, flow around long finite cylinders at $\mathrm{Re} = 100$ is investigated numerically using the incompressible Navier-Stokes Equations solver MGLET. To study the isolated flow near the free end, a cylinder with aspect ratio $^L/_D = 50$ is chosen. The flow over the free end gives rise to a wake consisting of two vortex shedding cells with different shedding frequencies; one small near the free end and one larger in the central region of the span. It is found that each vortex shed in the end cell bends horizontally and connects with the upstream vortex shed from the opposite side of the cylinder. The horizontal vortex shedding is found to give rise to a pair of trailing vortices in the time averaged flow.

When a vortex is shed with a large phase difference between the two cells, the vortex is split and connects with other surrounding vortices. This phenomena is commonly referred to as vortex dislocations and occurs with the beat frequency, i.e. the difference between the two vortex shedding frequencies. It is found that this frequency can be detected in time histories of u in the wake at the spanwise centre.

A second configuration, consisting of a wall mounted cylinder with aspect ratio $^L/_D = 25$ is simulated in order to study the effect of introducing a no-slip surface. The effect on the end cell is found to be minimal, while the central cell shedding frequency is reduced. Comparisons with published data on a cylinder with aspect ratio $^L/_D = 25$ and two free ends shows that both the reduction of aspect ratio and the introduction of the no-slip boundary condition contributes to the reduced shedding frequency.

Sammendrag

Viskøs strømning rundt sirkulære sylindre er en klassisk problemstilling i fluiddynamikken med mange praktiske anvendelser innen offshore teknologi. I strømning rundt sylindere av endelig lengde oppstår komplekse fenomener og koherente strukturer i vaken selv ved relativt lave Reynoldstall. En forståelse av naturen og dynamikken bak disse fenomenene kan danne grunnlag for bedre design og innovative løsninger for offshore og subsea konstruksjoner.

I den foreliggende studien er strømning rundt lange endelige sylindre med Re = 100 er undersøkt numerisk med den inkompressible Navier-Stokes ligningsløseren MGLET. For å studere den isolerte strømingen nær den frie enden er en sylinder med lengdeforhold $^L/_D = 50$ valgt. Den frie enden gir opphav til en vake bestående av to celler med ulik virvelavløsningsfrekvens; en liten celle nær den frie enden og en større i den sentrale regionen av spennet. Det er vist at virvelen avløst i endecellen bøyes horisontalt og kobles sammen med oppstrøms virvel avløst fra motsatt side av sylinderen. Den horisontale virvelavløsningen er funnet å gi opphav til et par av følgende virvler gjennomsnittstrømmen.

Når virvlen blir avløst med stor faseforskjell mellom de to cellene, oppstår virvelsplitting hvor hver ende og kobles med andre omkringliggende virvler. Dette fenomenet er ofte referert til som virveldislokasjoner og oppstår med beatfrekvensen, det vil si forskjellen mellom de to virvelavløsningsfrekvensene. Denne frekvensen er observert i en tidsserie av u i vaken ved sylinderens midtpunkt i lengderetning.

En annen konfigurasjon, bestående av en veggmontert sylinder med sideforhold $^L/_D = 25$ er simulert for å studere effekten av å innføre en no-slip randbetingelse. Effekten på endecellen er funnet å være minimal, mens virvelavløsningsfrekvensen i den sentrale cellen reduseres. Sammenligninger med publiserte data på en sylinder med lengdeforhold $^L/_D = 25$ og to frie ender viser at både reduksjon av lengdeforhold og innføring av en no-slip randbetingelse bidrar til å redusere virvelavløsningsfrekvensen.

NTNU
Norges teknisk-naturvitenskapelige universitet
Institutt for marin teknikk

HOVEDOPPGAVE I MARIN HYDRODYNAMIKK

VÅR 2012

FOR

Stud.techn. Pål Levold

STRØMNING OMKRING ENDELIG LANG SIRKULÆR SYLINDER
(Viscous flow around finite lenght circular cylinder)

Kandidaten skal gjøre numeriske simuleringer av viskøs strømning omkring en endelig lang sirkulær sylinder og kartlegge strømningsfeltet i waken.
Som en første del skal det gjennomføres en litteraturstudie omkring emnet. Både numeriske og eks-perimentelle resultater skal vurderes. Viktige parametere skal kartlegges. Særlig skal wake-strømningen studeres. Studier gjort med avkortede (truncated) sylindere kan også være til hjelp.
Lengde/diameter forhold, Re-tall og andre viktige strømningsparametere velges i samråd med veileder. Bruk av symmetrirelasjoner og effekt av grensebetingelser på strømningen, skal undersøkes.

Kandidaten skal gjøre direkte numeriske simuleringer (DNS) ved bruk av koden MGLET. Kandidaten skal sette seg inn i koden og spesielt redegjøre for viktige punkter knyttet til simulering av den aktuelle geometrien.
Visualisering av waken skal gjøres for å vise detaljer rundt endene på sylinderen. Viktige numeriske parametere skal dokumenteres. Gridkonvergering skal dokumenteres.

Kandidaten skal i besvarelsen legge frem sitt personlige bidrag til løsning av de problemer som oppgaven stiller. Påstander og konklusjoner som legges frem, skal underbygges med matematiske utledninger og logiske resonnementer der de forskjellige trinn tydelig fremgår. I besvarelsen skal det klart fremgå hva som er kandidatens eget arbeid, og hva som er tatt fra andre kilder.
Kandidaten skal utnytte de muligheter som finnes til å skaffe seg relevant litteratur for det problemområdet kandidaten skal bearbeide.
Besvarelsen skal være oversiktlig og gi en klar fremstilling av resultater og vurderinger. Det er viktig at teksten er velskrevet og klart redigert med tabeller og figurer. Besvarelsen skal gjøres så kortfattet som mulig, men skrives i klart språk. Den skal inneholde oppgaveteksten, forord, innholdsfortegnelse, sammendrag, hoveddel, konklusjon med anbefalinger for videre arbeid, symbolliste, referanser og eventuelle vedlegg. Alle figurer, tabeller og ligninger skal nummereres.
Det forutsettes at Institutt for marin teknikk, NTNU, fritt kan benytte seg av resultatene i sitt forskningsarbeid, da med referanse til studentens besvarelse.

Besvarelsen leveres i to eksemplar innen 11. juni 2012.

Bjørnar Pettersen
Professor

Faglig veileder: Stipendiat José Gallardo

Acknowledgements

I wish first and foremost to thank my supervisor, Professor Bjørnar Pettersen for introducing be to the fascinating subject of flow around finite cylinders and for the always inspiring and helpful guidance. His always enthusiastic attitude towards the field of fluid dynamics and helpful suggestions have been highly appreciated. I am also very thankful to PhD candidate José P. Gallardo Canabes for introducing me to MGLET and always helping me the times my simulations failed.

The simulations undertaken in the present study have been run on the supercomputers Njord and Ve. I am very grateful to NOTUR for granting me access to their compute facilities.

I would like to thank my office colleagues for a great year at Tyholt and, especially Torstein I. Bø, for valuable discussions on scientific writing. Further, I wish to thank my fellow student Rune Bjørkli for all the discussions and knowledge sharing on the topic of flow around cylinders.

Pål Levold
Trondheim, 2012

Contents

List of Figures

List of Tables

Nomenclature

C_D	Drag coefficient	-
$C_{D,amp}$	Non-dimensionalised drag amplitude	-
C_D^{max}	Maximum drag force coefficient	-
C_L	Lift coefficient	-
D	Cylinder diameter	m
f_D	Vortex dislocation frequency	hz
f_e	End cell vortex shedding frequency	hz
f_L	Central cell vortex shedding frequency	hz
L	Cylinder length	m
$^L/_D$	Aspect ratio	-
p	Pressure	Pa
Re	Reynolds number based on cylinder diameter	-
Re_x	Reynolds number based on distance across wall	-
$\boldsymbol{S}$	Symmetric part of velocity gradient tensor	$^1/_\mathrm{s}$
St	Strouhal number	-
St_D	Non-dimensionalised vortex dislocation frequency	-
St_e	Non-dimensionalised end cell vortex shedding frequency	-
St_L	Non-dimensionalised central cell vortex shedding frequency	-
u,v,w	Velocity components	$^\mathrm{m}/_\mathrm{s}$
U_∞	Inflow velocity	$^\mathrm{m}/_\mathrm{s}$
$\mathbf{v}$	Velocity vector	$^\mathrm{m}/_\mathrm{s}$

Δ	Minimum height between a minimum and a detected peak	
δ	Boundary layer thickness	m
μ	Dynamic viscosity	$^{kg}/_{s \cdot m}$
ν	Kinematic viscosity	$^{m^2}/_{s}$
$\mathbf{\Omega}$	Antisymmetric part of velocity gradient tensor	$^{1}/_{s}$
ρ	Fluid density	$^{kg}/_{m^3}$

Acronyms

FVM	Finite Volume Method
CFL	Courant–Friedrichs–Lewy
DNS	Direct Numerical Simulation
CFD	Computational Fluid Dynamics
IBM	Immersed Boundary Method
CPU	Central Processing Unit
HPC	High Performance Computing
MGLET	MultiGrid Large Eddy Turbulence
LES	Large Eddy Simulation

Chapter 1

Introduction

Viscous flow around a cylinder is a classic research topic in fluid dynamics and has a vast amount of practical applications. In marine technology, typical applications consists of the design of risers, pipelines and circular foundations. With the appearance of the laminar von Karman vortex shedding at Re > 40 (Sumer and Fredsøe [28]), the cylinder is subject to a harmonic cross flow force commonly referred to as the lift force. As the Reynolds number increases and the wake becomes turbulent, this lift force can become a severe challenge in engineering design.

In the analysis of for example an offshore riser, the cylinder is typically studied as either 2D or infinite. For many other applications, like industrial chimneys as an onshore example and circular foundations as an subsea example, the cylinder are of finite length and the boundary conditions are of interest. The introduction of these boundary conditions, typically a free end and a no-slip wall, introduces new flow phenomena which will be outlined in the sections to follow.

1.1 Vortex Dislocations and Oblique Shedding

The choice of boundary condition on the ends of a finite cylinder will affect the vortex shedding along the cylinder. Williamson [31] did an extensive experimental study of vortex shedding around finite cylinders and influence from the cylinder ends. For $64 <$ Re < 178, he identified a central cell with shedding frequency f_L and a smaller cell near each end with shedding frequency $f_e < f_L$. Williamson further reported that the end cell frequency f_e can be detected at the middle of the cylinder span for aspect ratios $L/D < 45$. This implies that for longer cylinders the central region is not directly affected by the vortex shedding at the ends.

Williamson also showed, as shown in Figure 1.1, that vortices in central cell are

shed with an oblique angle to the spanwise axis of the cylinder. This effect is caused by the presence of the cylinder ends and influences the central cell even for cylinder with spans of several hundreds diameters. As a result of the vortices' obliqueness, the shedding frequency will be altered and Williamson proposes the following relationship between the oblique shedding Strouhal number (St_θ) and the parallel shedding Strouhal number (St_0):

$$\mathrm{St}_0 = \frac{\mathrm{St}_\theta}{\cos(\theta)}, \tag{1.1}$$

where θ is the oblique shedding angle.

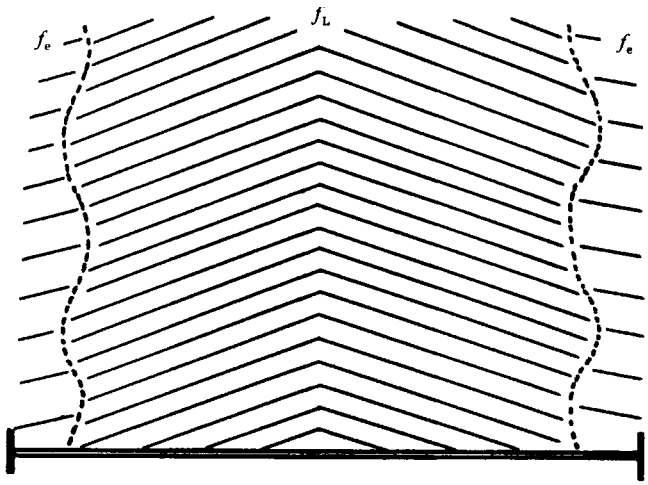

Figure 1.1: Chevron shaped oblique vortex shedding pattern. Figure from Williamson [31].

In the transition area between the two cells, Williamson observed a phenomena he called *vortex dislocations*: Due to the different shedding frequencies in the cells, the vortex shedding will at certain points in time be so much out of phase in the two cells that the vortex will split and merge with other surrounding vortices. These dislocations occur at the beat frequency between the two cells, i.e. at $f_D = f_L - F_e$.

1.2 Coherent Vortices

Much of the previous work on finite length cylinders have focused on identifying coherent flow structures. These structures can, especially at high Reynolds numbers, be difficult to identify by analysing instantaneous flow fields. The time averaged flow field is instead commonly used to identify coherent flow structures. Kawamura et al. [15] studied the flow around a finite wall mounted cylinder

experimentally and gave an overview of the wake flow features which is shown in Figure 1.2.

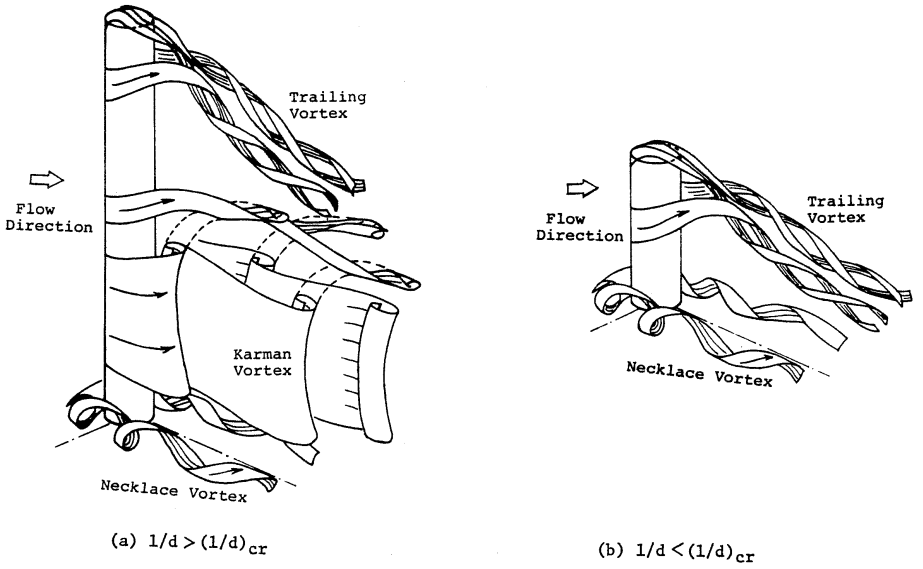

Figure 1.2: Overview of flow around wall mounted cylinder by Kawamura et al. [15].

1.2.1 Horseshoe Vortices

Some of the early experimental studies of the flow around a wall mounted cylinder was carried out by Baker [1, 2, 3]. He identified a horseshoe vortex system consisting of multiple vortices originating from in front of the wall-cylinder junction. These vortices wrap around the body moving downstream forming a U-shaped vortex system. In the laminar case Baker [1] identified vortex systems with 2, 4 and 6 individual vortices for increasing Re.

1.2.2 Trailing vortices

Kawamura et al. [15] focused their experimental investigations on the free end of a wall mounted finite cylinder. They identified two trailing vortices emerging from the free end of the cylinder. For aspect ratios less than a critical ratio $(L/D)_{cr}$ these vortices, in conjunction with the horseshoe vortex system, suppress the von Karman vortex street.

It was suggested by Roh and Park [26] that there actually is four trailing vortices originating from the free end. From visualisation experiments they drew two pairs

of counter-rotating vortices, where each vortex pair contains one vortex originating from the free end edge and one from the focal point at the free end surface. This proposition has been disputed by Pattenden et al. [23], Palau-Salvador et al. [21] and Krajnoviä [16] who all show that there is only a single pair of vortices originating from the free end.

1.2.3 Arch Vortex

Pattenden et al. [23, 24] identified, experimentally and numerically, a pair of tip vortices and an arch vortex in the near wake of a short wall mounted cylinder. This is shown in Figure 1.3 as a schematic drawing by Pattenden et al.

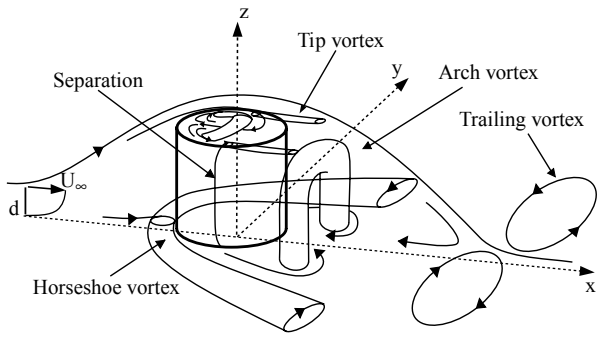

Figure 1.3: Schematic overview of flow behind a short wall mounted cylinder from Pattenden et al. [23].

Fröhlich and Rodi [7] showed that the tip vortices are joined together into the arch vortex just below the free end. This is not shown in Pattenden's figure, which otherwise gives a good summary of the flow features around a low aspect-ratio wall mounted cylinder.

1.3 Present Study

The present study undertakes the simulation and analysis of two finite cylinder, one with two free ends and aspect ratio $^L/_D = 50$ and one wall mounted cylinder with aspect ratio $^L/_D = 25$. These long aspect ratios are chosen to isolate the effect of the free end and the wall-cylinder junction. Both cylinders are simulated at a Reynolds number of 100 which is large enough to trigger vortex shedding, but still low enough to result in a laminar wake.

The outline of this document is as following:

Chapter 1 (this chapter) gives an introduction to flow around finite cylinders and the previous findings by other authors.

Chapter 2 outlines the numerical method used for the simulations as well as post processing techniques applied to the results.

Chapter 3 presents the setup and grids used for the simulations and the background for the choices made, including a grid convergence study.

Chapter 4 presents and discusses the results from the simulation of the cylinder with two free ends and $^{L}/_{D} = 50$.

Chapter 5 presents and discusses the results from the simulation of the wall mounted cylinder with $^{L}/_{D} = 25$. Comparisons to the results for the cylinder with two free ends and $^{L}/_{D} = 50$ are also made.

Chapter 6 finally summarises and concludes the findings and give recommendations for further work.

Chapter 2

Theoretical Background

This chapter presents the theory used in the present study. Section 2.1 gives a brief overview of the underlying theory used when simulating fluid flow in the present study. Some of the methods used by the chosen code are novel methods not commonly used in commercial codes and the advantages of these choices will be discussed. Finally, an overview of the post processing techniques used will be presented in Section 2.2.

2.1 Numerical Solution of the Navier Stokes Equations

The three dimensional, time-dependent and incompressible Navier-Stokes equations are to be solved:

$$\nabla \cdot \boldsymbol{u} = 0 \tag{2.1}$$

$$\frac{\partial \boldsymbol{u}}{\partial t} + \boldsymbol{u} \cdot \nabla \boldsymbol{u} = -\frac{1}{\rho}\nabla p + \nu \nabla^2 \boldsymbol{u} \tag{2.2}$$

In the present study, the Direct Numerical Simulation (DNS) and Large Eddy Simulation (LES) solver MultiGrid Large Eddy Turbulence (MGLET) (version `03-2011`) by Manhart et al. [19] has been used in DNS mode. The following sections will outline the methods used by MGLET. In the latest version of MGLET, some of the underlying methods have been changed, which means that it differs from what presented in the published literature. The changes and its implications will be made clear at the appropriate place in the following sections.

2.1.1 Spatial Discretization

For spatial discretization, MGLET uses the Finite Volume Method (FVM) where Equation (2.1) and (2.2) take the following integral form for a control volume (Day [5]):

$$\oint_S \boldsymbol{u} \cdot \boldsymbol{n} \, \mathrm{d}S = 0, \tag{2.3}$$

$$\frac{\partial}{\partial t} \int_V \boldsymbol{u} \, \mathrm{d}V + \oint_S \boldsymbol{u}(\boldsymbol{u} \cdot \boldsymbol{n}) \, \mathrm{d}S = - \oint_S p\boldsymbol{n} \, \mathrm{d}S + \oint_S \widehat{T} \cdot \boldsymbol{n} \, \mathrm{d}S, \tag{2.4}$$

where $\widehat{T} = \nu \left[\nabla \boldsymbol{u} + (\nabla \boldsymbol{u})^T \right]$, $\mathrm{d}V$ denotes integration over the control volume and $\mathrm{d}S$ denotes integration over the control surface.

For computational efficiency, MGLET utilises a non-equidistant Cartesian grid with a staggered arrangement for the flow variables as shown in Figure 2.1. For determining the cell face values of the velocities, linear interpolation is used while for the spatial derivatives ($\partial u / \partial x$ etc.) the central difference formula is used. This combination does, according to Manhart [20], provide second order accuracy.

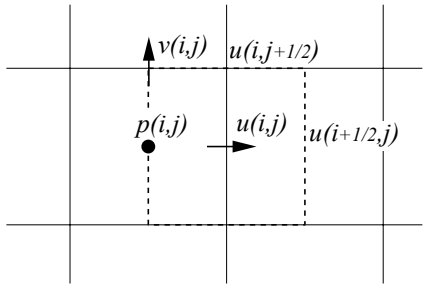

Figure 2.1: Staggered arrangement of flow variables from Manhart [20]. The solid lines indicate the cell for the pressure and the dashed lines indicate the velocity cell.

2.1.2 Temporal Discretization

MGLET uses the explicit third order Runge-Kutta scheme proposed by Williamson [32] to advance the simulation in time with the following procedure (Gallardo Canabes [10]). First, the pressure at the next timestep is found by solving the Poisson equation for the pressure change $\Delta p^{n+1} = p^{n+1} - p^n$:

$$\nabla^2(\Delta p^{n+1}) = \frac{\rho}{2\Delta t} \nabla \cdot \boldsymbol{u}^*, \tag{2.5}$$

where $\boldsymbol{u}^*$ is the velocity at an intermediate timestep calculated using Equation (2.2) with a time-lagged diffusion term from timestep $n-1$. Following Manhart [20], $\boldsymbol{u}^*$ is given by

$$\boldsymbol{u}^* = \boldsymbol{u}^{n-1} + 2\Delta t \left[\boldsymbol{u}^n \cdot \nabla \boldsymbol{u}^n + \nu \nabla^2 \boldsymbol{u}^{n-1} - \frac{1}{\rho} \nabla p^n \right] \tag{2.6}$$

The Poisson equation is solved iteratively with a divergence free velocity field, i.e. satisfying Equation (2.1), being the goal. A timestep computation is considered converged if the divergence of the velocity field is below a user set value $\nabla \cdot \boldsymbol{u} < \varepsilon$. Using superscript i as an iteration counter, one iteration comprises the following three steps:

$$\Delta p^{i+1} = \Omega \frac{\rho}{2\Delta t} \cdot \frac{1}{{}^1\!/\!_{\Delta x^2} + {}^1\!/\!_{\Delta y^2} + {}^1\!/\!_{\Delta z^2}} \tag{2.7}$$

$$u_j^{i+1} = u_j^i + \Delta p^{i+1} \frac{2\Delta t}{\Delta x_j} \tag{2.8}$$

$$p^{i+1} = p^i + \Delta p^{i+1} \tag{2.9}$$

Here, u_j is the three velocity components at the cell faces and Ω is an overrelaxation factor which is introduced in the pressure estimate (first step) to improve the convergence properties.

2.1.3 Immersed Boundary Method

As previously mentioned, MGLET uses a non-equidistant cartesian grid for its calculations. In order to introduce arbitrarily shaped solid bodies into the simulation, an Immersed Boundary Method (IBM) is applied: The body's no-slip boundary condition is transformed onto the grid by applying internal cell boundary conditions at the intersecting cells (Peller et al. [25]). For the intersecting cells, the velocities are prescribed (Dirichlet boundary condition) using interpolation with the surrounding cells and the intersecting no-slip condition. Figure 2.2 shows a 1D example where the following formula can be used to determine one of the velocity components in the intersecting cell, ϕ_0:

$$\phi_0 = \sum_{i=1}^{N} (\alpha_i \cdot \phi_i) + \alpha_r \cdot \phi_r \tag{2.10}$$

Here, α are the interpolation coefficients, N is the number of neighbouring cells used for the interpolation and subscript r denotes the values at the wall. An interpolation scheme of high order (i.e. large N), typically third or fourth order, is used to avoid requirements of an extremely fine grid near the body. Peller et al.

[25] further demonstrated that the interpolation coefficients (α_i and α_r) are only dependent on the geometry, i.e. x_r and x_i. This is a huge advantage in terms of efficiency because the coefficients can then be calculated in a pre processing step before the simulation.

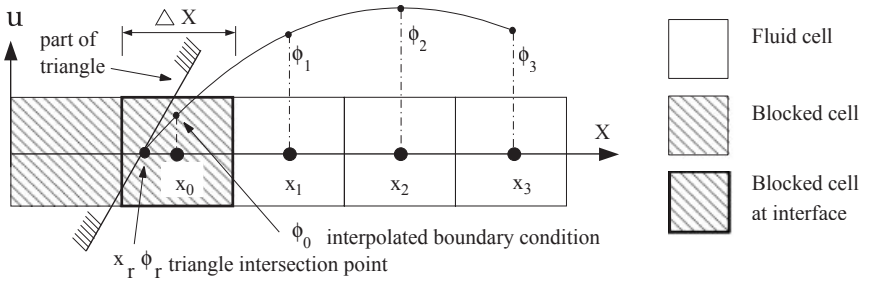

Figure 2.2: 1D interpolation near a no-slip boundary condition using the Immersed Boundary Method (IBM). Figure from Peller et al. [25].

To extend the IBM interpolation scheme into three dimensions, Peller et al. [25] used Equation (2.10) separately in three directions. The value of ϕ for each direction is then weighted according to a formula dependent on each direction's distance between the cell centre and the body intersection point.

This method outlined by Peller et al. [25] is the exact method used in older versions of MGLET. Due to issues with mass conservation, the method has been modified in the later version of MGLET which has been used in the present study (personal communication, Gallardo Canabes [8]). The new version does not use the same high order interpolation schemes described above, and it incorporates a flux correction to avoid mass imbalance.

The use of IBM makes MGLET able to simulate a vast range of fluid flow cases using a non-equidistant cartesian grid. Compared to more conventional methods that use a body-fitted grid, Manhart et al. [19] suggests that using a cartesian grid can reduce the Central Processing Unit (CPU) and memory usage between 10 and 30 times. This in turn allows for increased resolution and pushes the limits of what Re is practically possible to simulate on the available hardware.

2.1.4 Parallelization

While the computing power of CPU units are ever increasing, simulating viscous flow in a large domain using a serial code is generally not feasible. As for any other computational intensive task, the prevailing strategy is to run the calculations on multiple units. Thus, an important part of any modern Computational Fluid Dynamics (CFD) code is the ability to run efficiently in parallel.

MGLET was originally a serial code, but has lately been redesigned to run efficiently on massively parallel High Performance Computing (HPC) clusters. This is done

by dividing the computational grid into several smaller grids where each subgrid is treated in a serial manner (Manhart et al. [19]). This technique is called domain decomposition and is described by, among others, Winkelmann et al. [33]: Each subgrid is surrounded by a "halo" of cells corresponding to cells in the neighbouring subgrids. These have the flow variables from the surrounding subgrids and is updated at the appropriate times during the computation. A timestep for a single subgrid can thus be computed independently with the halo cells as boundary condition.

2.2 Post Processing Techniques

2.2.1 Vortex Identification with the λ_2-Criterion

One of the main goals of the present study is to analyse the vortex structures that form in the wake of a finite cylinder. There are several methods for visualising vortices in a flow field, one being the λ_2-criterion proposed by Jeong and Hussain [12]. The method divides the velocity gradient tensor $\nabla \boldsymbol{u}$ into a symmetric part ($\boldsymbol{S}$) and an antisymmetric part ($\boldsymbol{\Omega}$):

$$\boldsymbol{S} = \frac{1}{2}\left(\nabla \boldsymbol{u} + \nabla \boldsymbol{u}^T\right) \tag{2.11}$$

$$\boldsymbol{\Omega} = \frac{1}{2}\left(\nabla \boldsymbol{u} - \nabla \boldsymbol{u}^T\right) \tag{2.12}$$

The three eigenvectors of $\boldsymbol{S}^2 + \boldsymbol{\Omega}^2$ is then found and named such that $\lambda_1 \geq \lambda_2 \geq \lambda_3$. Jeong and Hussain show that vortices then can be identified by areas of negative λ_2 and provide several test cases to show the method's usability. In principle, anything inside an isosurface of $\lambda_2 = 0$ is identified as a vortex. To obtain more descriptive figures it is found more practical to plot an isosurface with a slightly negative λ_2 as this often reveals smaller details.

2.2.2 Analysis of Wake Fluctuations

To estimate the cell vortex shedding frequencies and other fluctuations occurring in the wake, a line of points can be placed in the wake in order to monitor the velocities u, v and w as well as the pressure p over time. The time series of a velocity or pressure signal at each point can then be analysed using Fast Fourier Transform to identify dominant frequencies. For one or a few points, the peaks in the frequency spectrum can be identified efficiently by manually inspecting the graph and extracting the frequencies from the data set. Doing this manually can indeed in many situations be more precise than using a computer algorithm because the human brain can see the data in a context that the computer generally cannot

and thus "filter out" certain peaks as noise. For a large amount of points however, this quickly becomes an unfeasible manual task in which case some sort of computer algorithm should be utilised.

The simplest form of peak detection is to search for points in the signal where both neighbouring points have a smaller value than the point itself. This will however detect every single peak which includes noise and low power peaks. Instead, the following method is proposed:

Considering a variable $\varphi(x, y, z, t)$ which is sampled with regular intervals in time at several points $(x_0, y_0, \boldsymbol{z})$ in space. The frequency spectrum for the signal of φ_i at a single point (x_0, y_0, z_i) can be found using Fast Fourier Transform and is denoted $|Y_i(f)|$. Instead of finding every single peak as discussed above, the code made publicly available by Billauer [4] is used. For a point to qualify as a peak using this algorithm, the height difference between the point and a point in its neighbourhood must be larger than a prescribed value Δ. This means that between each *detected* peak there must be a valley lower than Δ from the smaller of the two peaks. This should eliminate noise and less dominant peaks. The peak detection is then repeated for all z_i.

The results of this method will depend on the choice of Δ which there is no exact rule for. After some trial and error in conjunction with manual inspection of some frequency spectra it was found that $\Delta = 0.02$ seems to detect most of the important peaks, however, this will vary for different use cases.

2.2.3 Force Coefficients

MGLET calculates the global forces acting on the body flow is simulated around. From the force history of the stable part of a simulation, the drag coefficient is calculated from the average of the force in x-direction:

$$C_D = \frac{\overline{F_x(t)}}{1/2 \rho U_\infty^2 LD} \tag{2.13}$$

The coefficient of the drag force amplitude is the difference between the maximum and mean drag force:

$$C_{D,amp} = \frac{\max_t F_x(t) - \overline{F_x(t)}}{1/2 \rho U_\infty^2 LD} \tag{2.14}$$

The lift coefficient is calculated using the maximum value of the force in y-direction:

$$C_L = \frac{\max_t F_y(t)}{1/2 \rho U_\infty^2 LD} \tag{2.15}$$

Chapter 3

Computational Setup

This chapter discusses the grid and simulation parameters used in the present study. First, a set of 2D simulations which have been used to determine an adequate domain size and grid spacing are presented. Using these simulations as a basis, the grid is then extended into two 3D grids which have been used for the simulations presented in the next chapters.

All simulations carried out in the present study is on Re = 100. This is achieved in MGLET by setting the inflow velocity (U_∞), the cylinder diameter (D) and the fluid density (ρ) to unity. The Reynolds number is then given by

$$\mathrm{Re} = \frac{\rho U D}{\mu} = \frac{1}{\mu}. \tag{3.1}$$

Thus, Re = 100 can be achieved by setting the fluid viscosity (μ) to 0.01.

3.1 Domain Size

When simulating external, flow the choice of domain size is important as it should be large enough not to cause blocking effects. When simulating flow around a cylinder there are two domain dimensions of particular interest: The distance from the inlet to the cylinder and the distance between the domain sides and the cylinder. In Figure 3.1, which presents the domain schematically, these dimensions are denoted X_1 and Y_1 respectively.

To determine an adequate domain size in terms of X_1 and Y_1, simulations were run on a fine grid ($\Delta x = 0.01$ near the cylinder) with different choices of X_1 and Y_1. The same fine grid will later be used for the grid dependence study as the case with the finest grid sizes. While this increases the computation time for the blockage

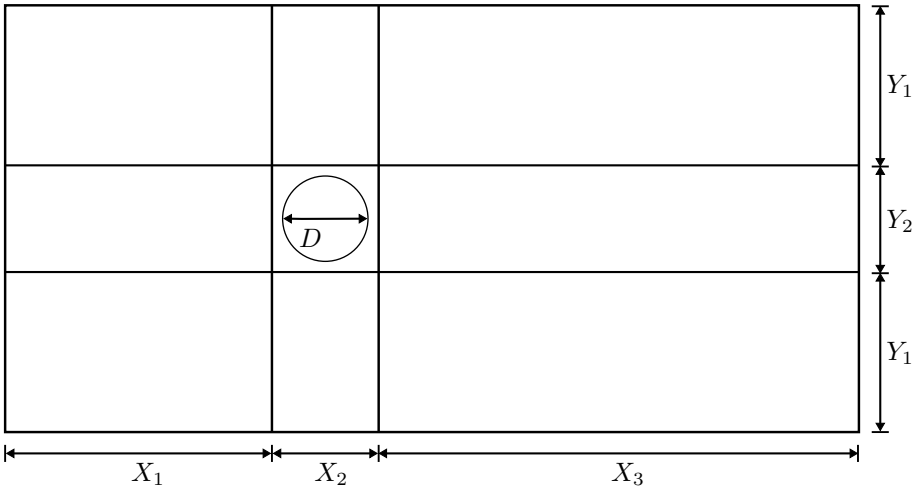

Figure 3.1: Domain sizes for flow around 2D cylinder. The same domain is extended in z-direction for the 3D simulations.

study, it does ensure that the grid size does not affect the results significantly.

The following parameters are measured over a period of time after the simulation has reached a steady state:

- St: The Strouhal frequency is determined using Fast Fourier Transformation of the lift force signal.
- St_x: The non-dimensionalised drag force frequency is found using Fast Fourier Transformation.
- C_L: The lift calculated as specified in Section 2.2.3.
- C_D^{max}: The maximum drag coefficient is found using the overall maximum value of the drag force.

The convergence of a variable ϕ for a simulation i is then determined by

$$\text{Convergence}_{\phi_i} = \left| \frac{\phi_i}{\phi_n} - 1 \right|, \tag{3.2}$$

where n denotes the assumed best simulation, i.e. the simulation with the finest grid or the largest domain. This means that the convergence for the assumed best simulation by definition is zero. For other simulations, a value close to zero will indicate that the simulation has good accuracy compared to the assumed best.

All the previously mentioned variables which are calculated for each simulation use the forces acting on the cylinder as a basis. The forces are calculated by integrating

the pressure and shear stress on the body, which in itself can lead to inaccuracies. Ideally some non-integrated variables, like the cross flow velocity at a point in the wake, should also have been analysed in order to give a better overall impression of the convergence. The velocities at different points in the wake were indeed measured during the simulations but proved problematic to export afterwards and had to be omitted.

Table 3.1 and Figure 3.2 show the results for different values of X_1. While the values of the frequency parameters are relatively inaccurate for short X_1, they quickly converge to the same number with larger accuracy than shown in Table 3.1. On the other hand, the lift and drag coefficients converges slowly and even when going from $X_1 = 16$ to $X_1 = 18$ there is still some change. Force calculations are however not the main goal of the present study so $X_1 = 16$ is chosen.

Table 3.1: Effect of distance between inlet and cylinder, X_1, on lift and drag.

X_1	Y_1	St	St_x	C_L	C_D^{max}
4	7	0.1800	0.3600	0.3553	1.4780
6	7	0.1744	0.3488	0.3575	1.4326
10	7	0.1800	0.3400	0.3392	1.4045
16	7	0.1735	0.3367	0.3392	1.3980
18	7	0.1739	0.3369	0.3402	1.3956

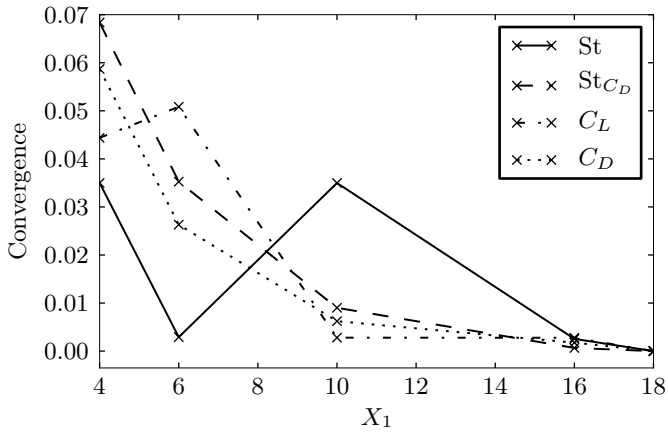

Figure 3.2: Convergence of 2D cylinder case against distance between inlet and cylinder, X_1.

Using $X_1 = 16$, the value of Y_1 was varied as shown in Table 3.2 and Figure 3.3. Here, all the parameters converge for $Y_1 = 10$ which is thus chosen for use in the final grid. This corresponds well with Zdravkovich [34, Chapter 23] who states that the blockage effect for a cylinder near a wall may be ignored if the gap $^B/_D > 10$. In his case, the boundary is a no-slip wall compared to a free-slip wall in the present

simulations, which means that this choice should be large enough to avoid blockage effects.

Table 3.2: Effect of distance between domain side and cylinder, Y_1, on lift and drag.

X_1	Y_1	St	St_x	C_L	C_D^{max}
16	7	0.1735	0.3367	0.3392	1.3980
16	10	0.1714	0.3428	0.3323	1.3747
16	14	0.1714	0.3428	0.3323	1.3747

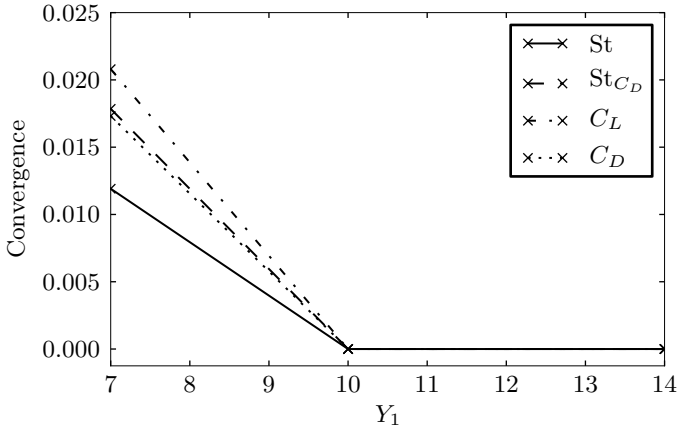

Figure 3.3: Convergence of 2D cylinder case against distance between domain side and cylinder, Y_1.

3.2 Grid Dependence Study

With the domain dimensions established, the grid dependence can be studied to chose a suitable grid spacing for the simulations. The grid spacing on the boundaries are kept approximately constant while the grid spacing around the cylinder (Δx) is varied. The cells around the cylinder are made square so that $\Delta y = \Delta x$.

All of these simulations are run at the same time step, $\Delta t = 0.002$ which was necessary for the case with $\Delta x = 0.01$ to converge. This was not necessary on the coarser grids, but the same time step is used in all simulations to limit the amount of variables changed between each simulation.

As seen from Table 3.3 and Figure 3.4, all the chosen parameters have converged, with two digits precision, when $\Delta x = 0.02$. Using such fine grid will however lead to long computation times since the computation time generally follows $\mathrm{O}(N^3)$,

where N is the number of cells. A grid spacing of $\Delta x = 0.05$ was chosen as a trade-off between computational time and accuracy. Looking at Figure 3.4 however, choosing $\Delta x = 0.04$ or less would probably be better as the parameters are still varying with the grid size.

Table 3.3: Effect of grid spacing (Δx) near cylinder on lift and drag.

Δx	St	St_x	C_L	C_D^{max}
0.10	0.1600	0.3200	0.2571	1.3371
0.05	0.1750	0.3250	0.3056	1.3683
0.02	0.1714	0.3428	0.3302	1.3740
0.01	0.1714	0.3428	0.3323	1.3747

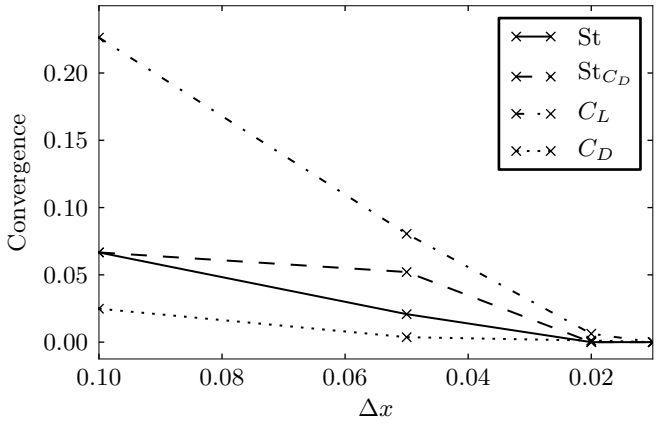

Figure 3.4: Convergence of 2D cylinder case for different grid spacings, Δx, near cylinder.

Due to the low time step used in these simulations, the Courant–Friedrichs–Lewy (CFL) number is generally well within what is necessary for the numerical method to be stable. For the 3D simulations, the time step is increased to $\Delta t = 0.01$ which is still found to give sufficient CFL numbers. Table 3.4 compares results for the 2D cylinder using both time steps and while some change in the measured parameters are observed, the increased time step seems justifiable.

Kravchenko et al. [17] studied the flow around a 2D cylinder at Re = 100 and provided an extensive convergence study for several parameters which is compared to the present study in Table 3.4. The present results show generally larger values compared to their results, but no major differences are seen.

Table 3.4: Comparison of 2D cylinder results with different time steps to results from Kravchenko et al. [17].

Author	Case	St	C_L	C_D^{max}
Kravchenko et al. [17]		0.1640	0.3140	1.3140
Present study	$\Delta t = 0.002$	0.1714	0.3323	1.3747
	$\Delta t = 0.01$	0.1700	0.3056	1.3684

3.3 Three Dimensional Grid

Two different cases are simulated in the present study; the first being a cylinder with two free ends and $^L/_D = 50$ and the second being a wall mounted cylinder with $^L/_D = 25$. By utilising a symmetry boundary condition, which will be discussed in the next section, the same computational domain is used for both cases. For the wall mounted cylinder, the grid near the wall has been refined to resolve the boundary layer.

One of the objectives of the present study is to investigate the isolated effect of the free end. To achieve this it is necessary that the cylinder is long enough for the two ends not to interfere. As previously mentioned, Williamson [31] found that the central areas of a finite cylinder are not directly influenced by the ends when $^L/_D > 45$. If the central area of the cylinder span is not directly influenced by the ends, it is not unreasonable to apply a symmetry condition at the middle of the cylinder. This was done by Inoue and Sakuragi [11] for $^L/_D \geq 50$ and the same setup is chosen here for the cylinder with two free ends and $^L/_D = 50$.

The distance between the free end of the cylinder and the top of the simulation domain is set to be $5.5D$ long. This is approximately the same as used by Palau-Salvador et al. [21]. Krajnoviä [16] and Inoue and Sakuragi [11] on the other hand, used a gap of $16D$ and $30D$ respectively so it is likely that this choice will cause blocking and affect the results.

Figure 3.5 shows every fourth grid line in the xy plane, where the domain dimensions and grid spacing obtained in the previous sections have been used. Similarly, Figure 3.6 shows every fourth gridline in the xz plane for the cylinder with two free ends and $^L/_D = 50$. In the central regions of the cylinder span, the vertical velocities behind the cylinder are expected to be low compared the velocities in x and y directions. The grid spacing can thus be relaxed in this region and a spacing of $\Delta z \approx 0.1$ is chosen at $z = 0$. Near the free end, where the vertical velocities are expected to increase due to the flow over the free end, grid spacing is gradually decreased down to $\Delta z = 0.05$. Figure 3.7 shows every fourth gridline in the xz plane for the wall mounted cylinder. The grid is the same in this plane as for the cylinder with two free ends, with the exception of a refined region of $\Delta z = 0.05$ near the wall boundary at $^z/_D = 0$. Above this region, the grid spacing is gradually relaxed up to $\Delta z \approx 0.1$ like for the cylinder with two free ends.

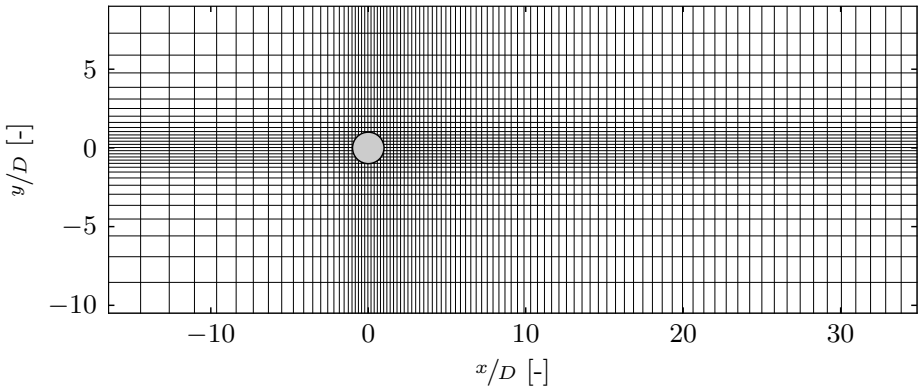

Figure 3.5: Slice of computational grid in xy plane.

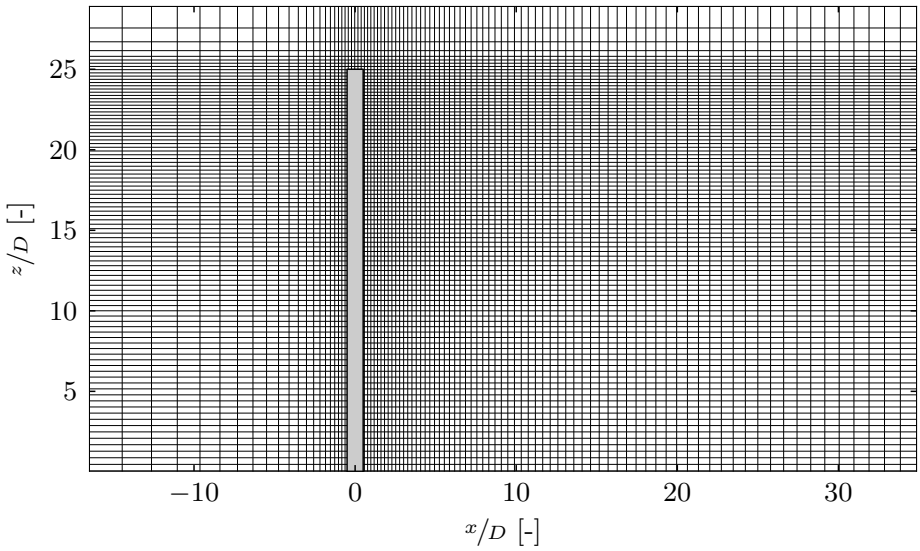

Figure 3.6: Slice of computational grid for cylinder with two free ends and $L/D = 50$ in xz plane.

The grids used in the present study are very fine and the performance could probably have been improved significantly without influencing the accuracy. Both grids have $388 \cdot 132 \cdot 388 \approx 19.87 \times 10^6$ cells, including two layers of extra cells outside the domain used by MGLET for enforcing boundary conditions. To reduce the total number of cells, Δz in the central regions of the cylinder span could be relaxed further. Also, the grid resolution in the cylinder wake is very fine compared to the large scale wake structures occurring at $\mathrm{Re} = 100$.

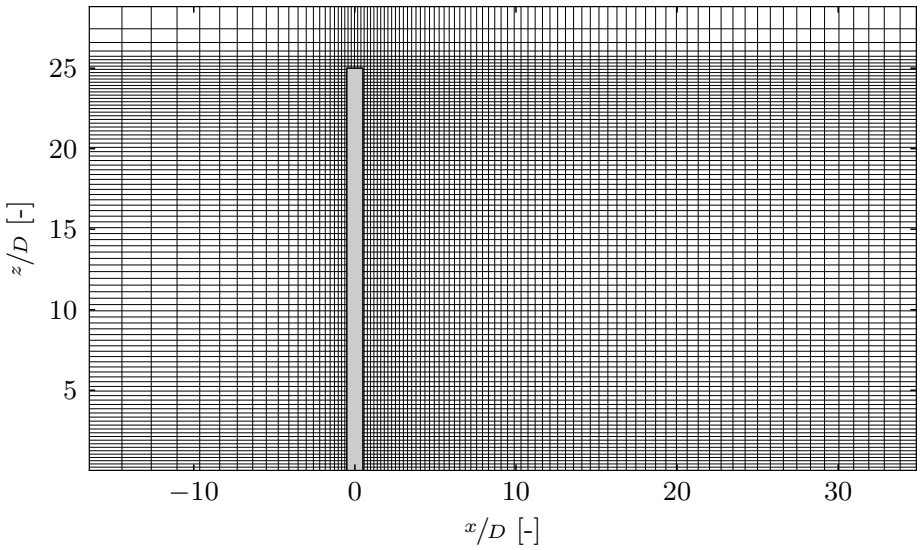

Figure 3.7: Slice of computational grid for wall mounted cylinder with $L/D = 25$ in xz plane.

3.4 Boundary Conditions and Initial Conditions

There are two types boundary conditions used in a CFD simulation; a Dirichlet condition, where the value of one or more of the flow variables (u, v, w and p) is prescribed and a Neumann condition, where the derivatives are prescribed. To be able to solve the governing equations, a boundary condition has to be applied for each flow variable at the boundaries. Each of the sides in the rectangular computational domain and their corresponding boundary condition are listed in Table 3.5.

Table 3.5: Summary of boundary conditions applied at the domain sides. "Case 2" denotes the simulation with a wall mounted cylinder.

Boundary	Type	Dirichlet Condition	Neumann Condition
Upstream end	Inlet	$\boldsymbol{u} = U_\infty \boldsymbol{i}$	$\partial p/\partial x = 0$
Downstream end	Outlet	$p = 0$	$\partial \boldsymbol{u}/\partial x = 0$
Vertical sides	Free-slip	$v = 0$	$\partial u/\partial y = \partial w/\partial y = \partial p/\partial y = 0$
Top side, bottom side	Free-slip	$w = 0$	$\partial u/\partial z = \partial v/\partial z = \partial p/\partial z = 0$
Bottom side, case 2	No-slip	$\boldsymbol{u} = 0$	$\partial p/\partial x = 0$

The cylinder with two free ends and $L/D = 50$ is modelled with a symmetry condition at $z/D = 0$. This is done by setting the boundary condition at the bottom side to a free-slip wall in MGLET. Since a free-slip wall allows no fluid to

pass through, but allows the fluid to flow along the surface, a free-slip surface and a symmetry plane is two names for the same boundary condition.

In addition to a set of boundary conditions, it is necessary to define an initial condition for each cell. This is done automatically by MGLET by setting each variable to zero in each cell.

Chapter 4

Results and Discussion: Cylinder with Two Free Ends

The results presented here were obtained by simulating a cylinder with two free ends as described in Section 3.3. From the initial conditions, the simulation was first run until it reached a steady state. After reaching a steady state, the simulation was run for several shedding periods to obtain the time series and statistics used in this chapter.

Instantaneous flow field data were sampled every second from a time series of $\tau = 30$. Unfortunately, MGLET does only support exporting flow field data at the end of a simulation and not at certain time steps during the run. To obtain a time series of flow fields MGLET's restart facility was utilised. A series of $\tau = 1$ (flow time) long simulations were run and the flow field was exported. The flow field from the previous simulation was then used to initialise the next simulation. This procedure was repeated programatically 30 times resulting in a sequence of 30 flow fields. Scripts, input files and additional visualisations for these simulations can be found in the electronic appendix (see Appendix A.1 for an overview).

4.1 Vortex Shedding Pattern

To give an overview of the wake structure, an isosurface of λ_2 for a time instant is shown in Figure 4.1. The upper half of the vortex shedding pattern that Williamson [31] described as a chevron shaped pattern can clearly be observed from the plane of symmetry and up. Downstream of the cylinder, in the end cell, the vortices are bent horizontally and through the $y = 0$-plane. This part of the vortices have a shape that is similar to one of the halves of a hairpin vortex which for example Johnson and Patel [13] observed in the flow behind a sphere. The same kind of

hairpin vortices was also observed by Inoue and Sakuragi [11] behind a cylinder with $^{L}/_{D} < 10$ at Re $= 100$. It is also observed that these vortices propagate downstream a distance below the free end, which means that the vortex shedding is suppressed in the part of the span nearest the free end.

Figure 4.2 shows the same λ_2-isosurface with a top-down view. From this view, one can see that each horizontal part of the vortices overlap the tail of the preceding vortex. In this region, a clockwise rotating vortex is connected with a counterclockwise vortex as shown more clearly in Figure 4.3. The counterclockwise vortex also extend backwards and the same pattern occurs again on the other side of the $y = 0$ plane. This corresponds well with Helmholtz's second theorem for an invicid fluid (see e.g. Kambe [14, Chapter 7]):

> *A vortex filament cannot end in a fluid; it must extend to the boundaries of the fluid or form a closed path.*

Helmholtz's second theorem is not strictly true for a real fluid because vortices many dissipate due to viscosity, but it is useful as an approximate explanation of phenomenas in low-Re flows (see e.g. Dunn and Tavoularis [6]). In this case, two oblique vortices extend from the $z = 0$ plane and connect in the end cell. Due to the symmetry boundary this essentially means that there is a vortex core forming a closed loop between the two free ends of the cylinder. Since each vortex connects with its upstream counterpart, a chain of vortex loops are formed and this is drawn schematically in Figure 4.4.

Close to the downstream end of the domain in Figure 4.1, it is observed that a counterclockwise vortex has split in the central cell and connected with a clockwise vortex. Although not shown here, snapshots from earlier in the sequence show that the splitting of this vortex was present when it was further upstream as well. This is the phenomena referred to by Williamson [31] as vortex dislocations and will be discussed further in Section 4.5.

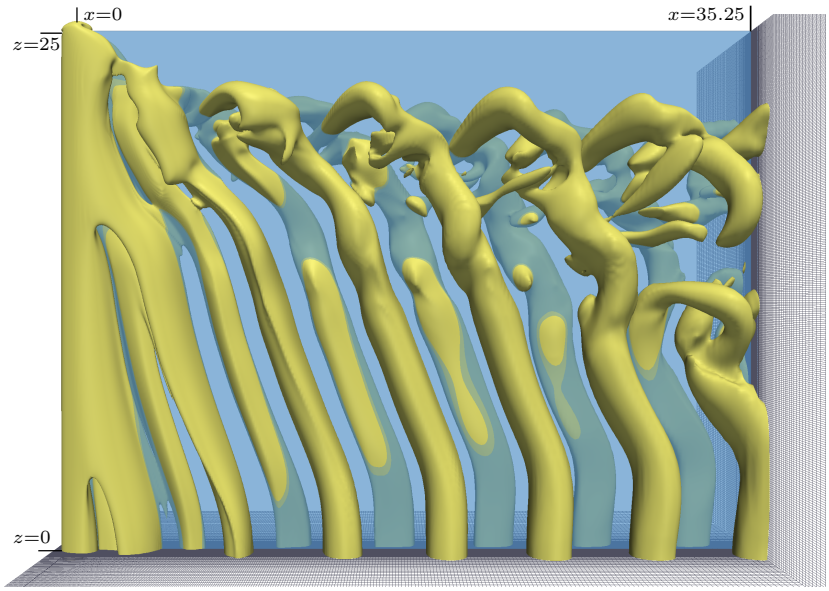

Figure 4.1: Isosurface of $\lambda_2 = -0.01$ for cylinder with two free ends and $^{L}/_{D} = 50$. The semitransparent cyan plane is located at $y = 0$ to give an indication of the vortex location in y-direction. U_∞ flows along positive x-axis and symmetry plane ($z = 0$) is at the bottom of the figure.

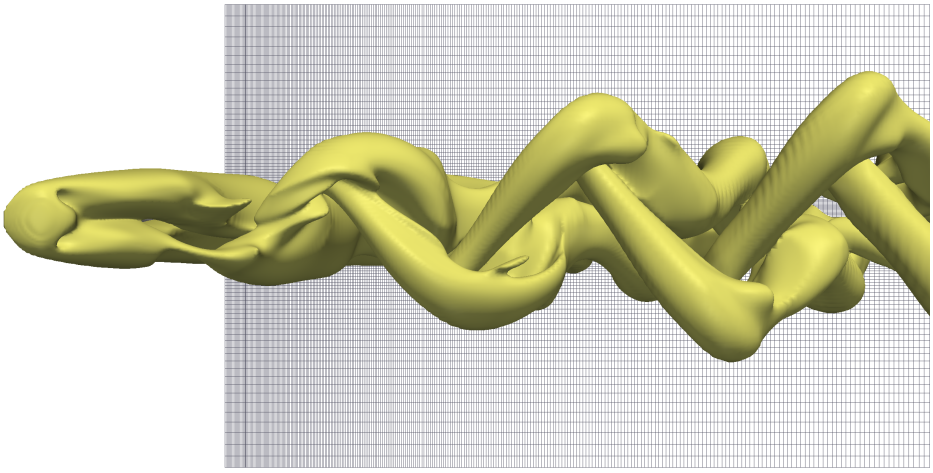

Figure 4.2: Top view of $\lambda_2 = -0.01$ isosurface for cylinder with two free ends and $^{L}/_{D} = 50$.

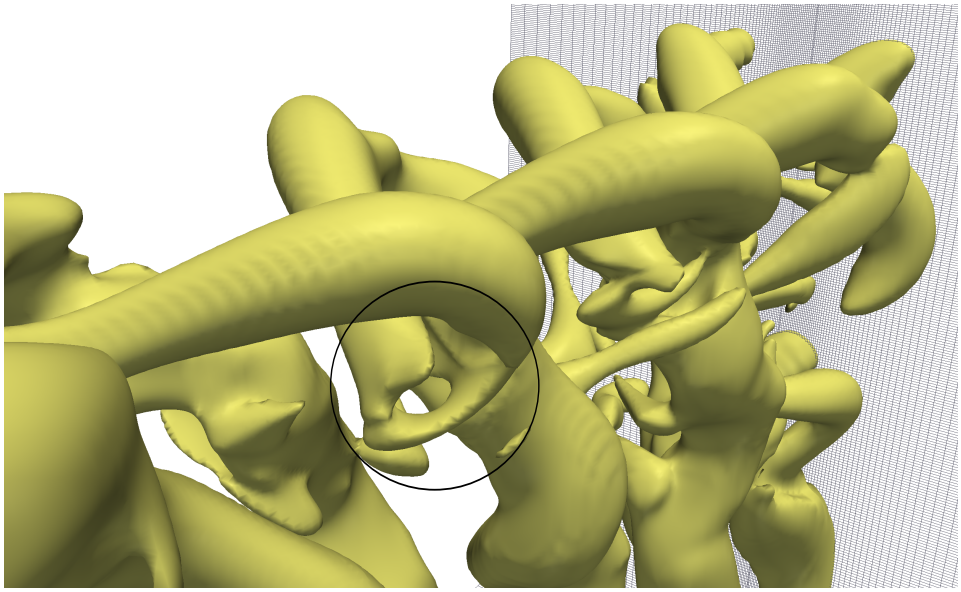

Figure 4.3: Isosurface of $\lambda_2 = -0.01$ showing closeup of overlapping horizontal vortex filaments. The black circle shows the connection between the clockwise and the counterclockwise vortex.

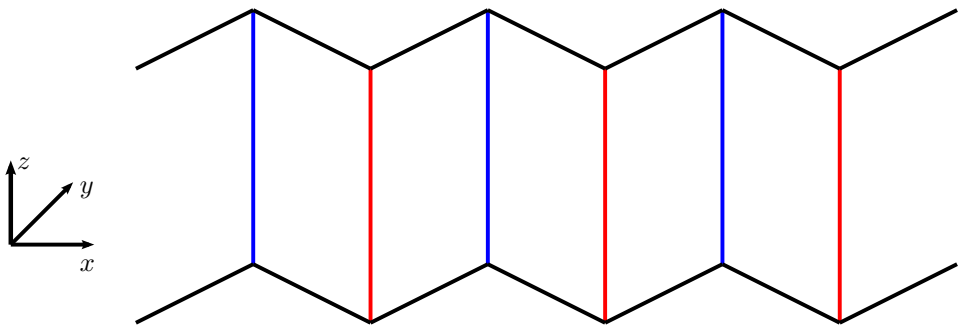

Figure 4.4: Schematic description of vortex shedding from a cylinder with two free ends. Blue lines indicate clockwise vortices shed from the positive y side of the cylinder, red lines indicate counterclockwise vortices shed from the positive y side of the cylinder and black lines indicate the horizontal parts of the vortices connecting the horizontal vortices together. Note that the vertical and horizontal lines are not to scale.

4.2 Flow Over Free End

From simulations on high Re, Pattenden et al. [23], Palau-Salvador et al. [21] and Krajnoviä [16] all identified a separation bubble above the free end of the cylinder. As seen in Figure 4.5, which shows in-plane velocity vectors in the $y = 0$ plane, this is not the case at $\mathrm{Re} = 100$. Here, the fluid flows in a laminar boundary layer above the free end, and no separation occurs.

Above the cylinder there is a region where the horizontal velocity rapidly increase towards a maxima before gradually decreasing toward U_∞. This is better seen in Figure 4.6, which shows the u-velocity profile at the cylinder centre. The shape of the velocity profile is similar to the profile perpendicular to the cylinder wall which also reaches a maximum close to the wall before approaching U_∞. From Figure 4.6 it should also be noted that at the domain boundary (the top of the figure), $u \neq U_\infty$ which means that blocking effects could influence the results.

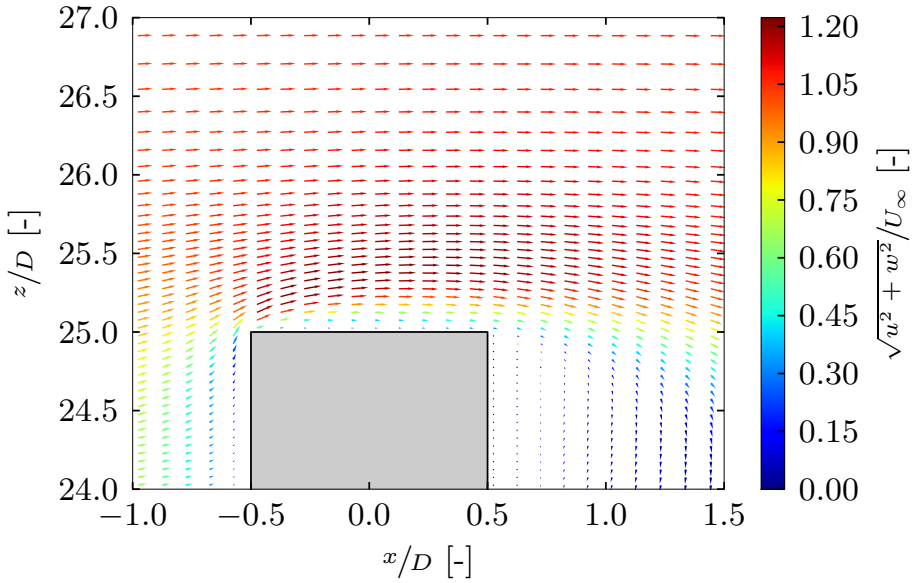

Figure 4.5: In-plane velocity vectors in the $y = 0$ plane around the free end.

From Figure 4.7, which shows contours of u in the $y = 0$ plane near the fee end, it can be observed that the distance from the cylinder to the u maxima is increasing along the cylinder diameter. While this is by no means a regular Blasius boundary layer (see e.g. White [29]), it shares the same basic principle that its height increases as the distance from the upstream end of the cylinder increases.

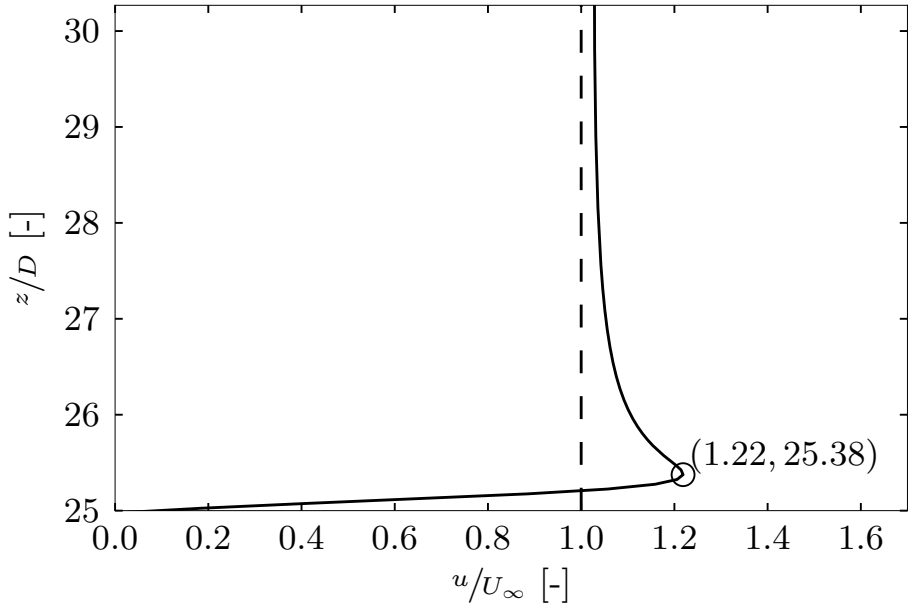

Figure 4.6: Horizontal velocity profile above the centre of the cylinder free end. The position of the maximum is marked with a circle and its coordinates.

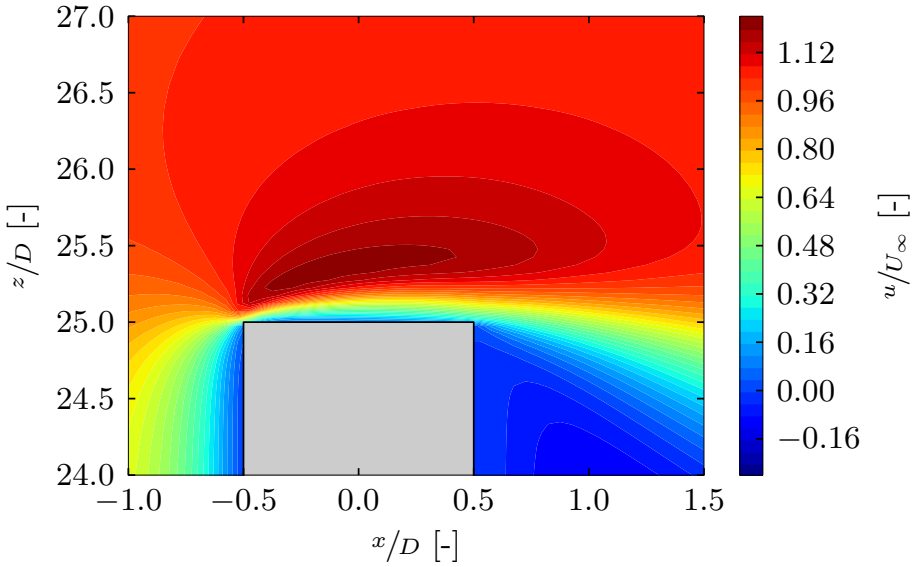

Figure 4.7: Contour of u near cylinder free end.

4.3 Arch Vortex

As discussed in Section 1.2.2, other authors have identified an arch vortex in the mean flow behind the cylinder at higher Re. At Re = 100, this vortex does also appear clearly in the instantaneous flow. Its centre is at the cylinder centreline, which is shown in Figure 4.8, from which it extends down in two oblique arms behind the cylinder. Comparisons between visualisations using the instantaneous flow field and visualisations using the mean flow field show that the arch vortex centre is stationary.

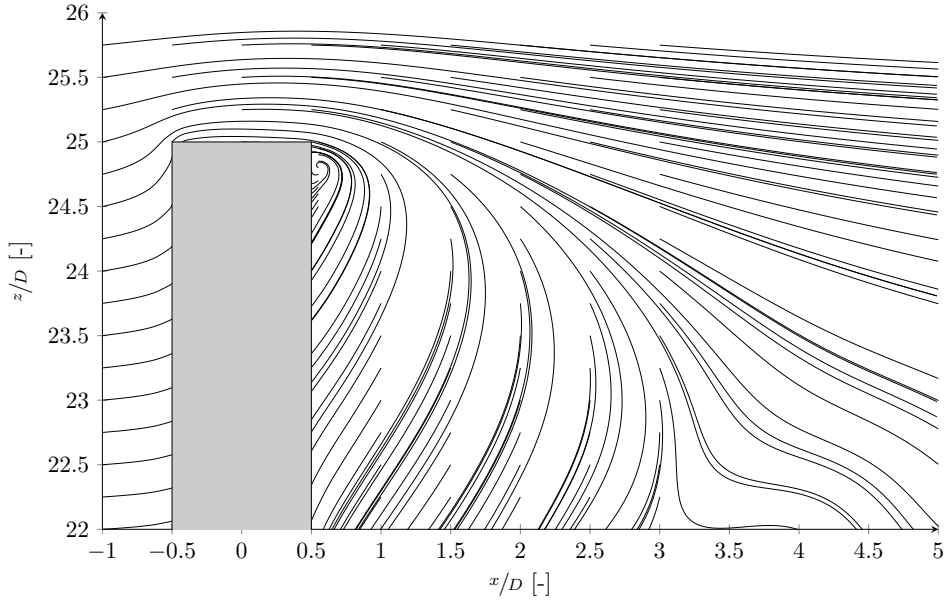

Figure 4.8: Arch Vortex centre

The arch vortex is a fairly weak vortex which makes it difficult to visualise using the λ_2-criterion. Several values of λ_2 were tried in order to visualise the vortices near the free end, but no satisfactory result were obtained. The λ_2-criterion performs well visualising the large and strong vortices, but it seems that these vortices dominate the results leaving the arch vortex difficult to identify. Streamlines were found to be the best method to visualise the arch vortex, however care should be taken when placing the initial points in order to achieve a good result.

Figure 4.9 shows a sequence of approximately one cycle of vortex shedding from the free end starting with $\tau' = 0$. The arch vortex is visualised with blue streamlines emitted from the sides of the cylinder at $(x, y) = (0, \pm 0.5D)$ and red streamlines emitted from the back of the cylinder at $(x, y) = (0.6D, \pm 0.1D)$. λ_2 is used to visualise the vortex shedding in the end cell which encapsulates the arch vortex.

Starting at $\tau' = 0$, an end cell vortex is being shed from the negative y side of the cylinder (the same side as the viewpoint). From $\tau' = 0$ to $\tau' = 2$, this end cell vortex moves further downstream and the blue streamlines from the negative y side as well as all but one red streamline follows the vortex downstream. At $\tau' = 4$ the same end cell vortex is about to detach from the cylinder's free end and the streamlines have moved back close to the cylinder. All but one red streamline have now moved to the other side of the cylinder and is about to follow the end cell vortex shedding from the positive y side of the cylinder. These visualisations show that both arch vortex arms persist during the whole free end shedding cycle, but with varying strength depending on which side a vortex is shed from.

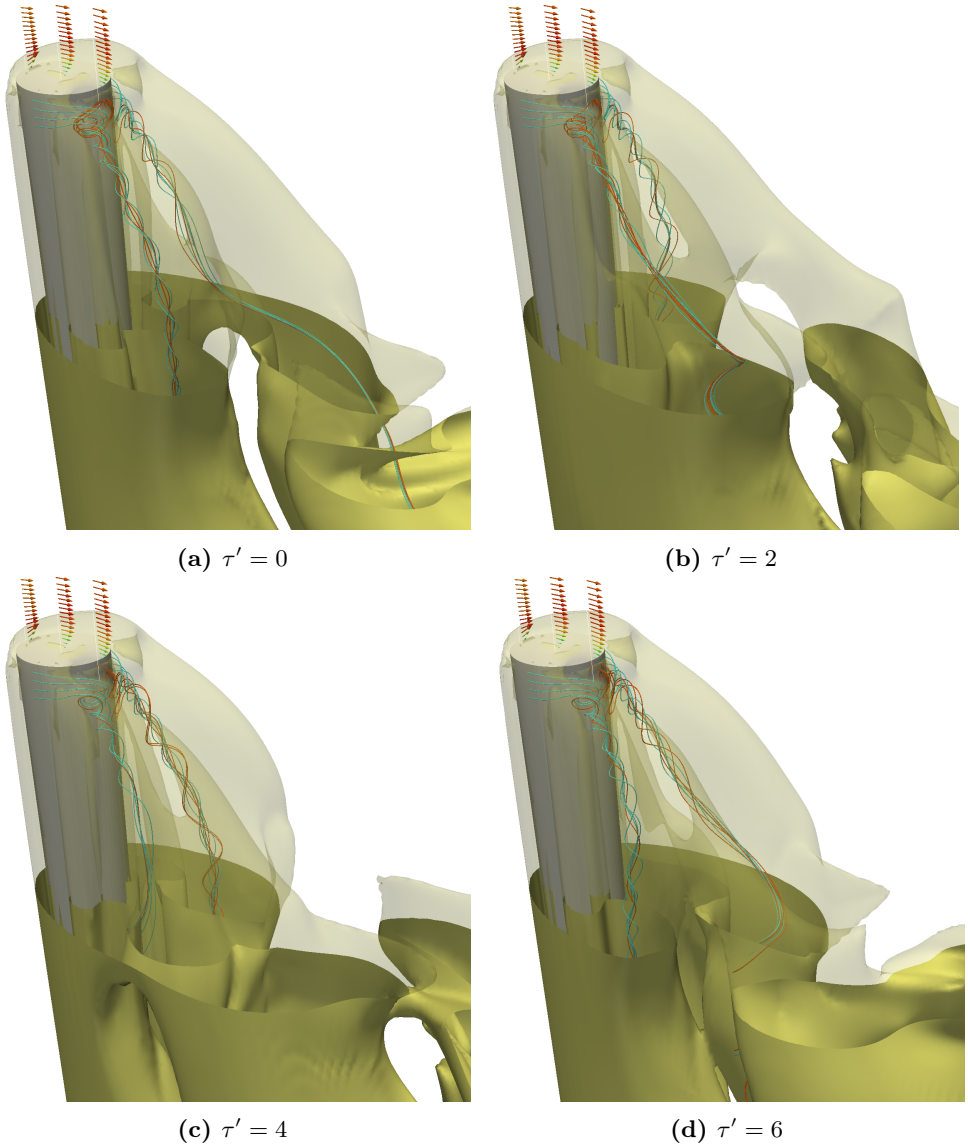

(a) $\tau' = 0$ **(b)** $\tau' = 2$

(c) $\tau' = 4$ **(d)** $\tau' = 6$

Figure 4.9: Arch vortex visualised by streamlines. Four blue streamlines are emitted from each side of the cylinder at $(x, y) = (0, \pm 0.5D)$, three red streamlines are emitted from $(x, y) = (0.6D, 0.1D)$ and three from $(x, y) = (0.6D, -0.1D)$. All streamlines are emitted within the range of $24.4 \leq {}^{z}/_{D} \leq 24.9$. The isosurface of $\lambda_2 = -0.01$ is shown in yellow and made semitransparent near the free end to show the streamlines. Some velocity vectors are rendered above the free end to give an impression of the flow direction. Non-dimensionalised flow time relative to the first image is shown below each image.

4.4 Mean Flow Field

The time averaged flow field, or mean flow field, is helpful to identify coherent structures in an unsteady flow. Periodic structures like the oblique vortex shedding identified earlier in this chapter will not appear in these results, but other authors have identified mean wake structures like a pair of trailing vortices behind the free end (see Section 1.2) for higher Re.

Using the λ_2-criterion, Figure 4.10 shows a pair of trailing vortices emerging in the near wake at a few diameters below the free end. The trailing vortices appear to be weak compared to the oblique vortex shedding and a value of $\lambda_2 = -0.005$ was necessary to visualise the whole vortex compared to $\lambda_2 = -0.01$ which was used in Section 4.1.

The trailing vortices are located in the end cell of the cylinder and are caused by the nearly horizontal part of the vortices shed from the free end. This is seen clearly in Figure 4.11 where an isosurface of the mean λ_2 is superimposed over λ_2 for the same time instant as in Figure 4.1. Here, the position trailing vortices can be observed to be in the region where the end cell vortices bend over to being approximately horizontal.

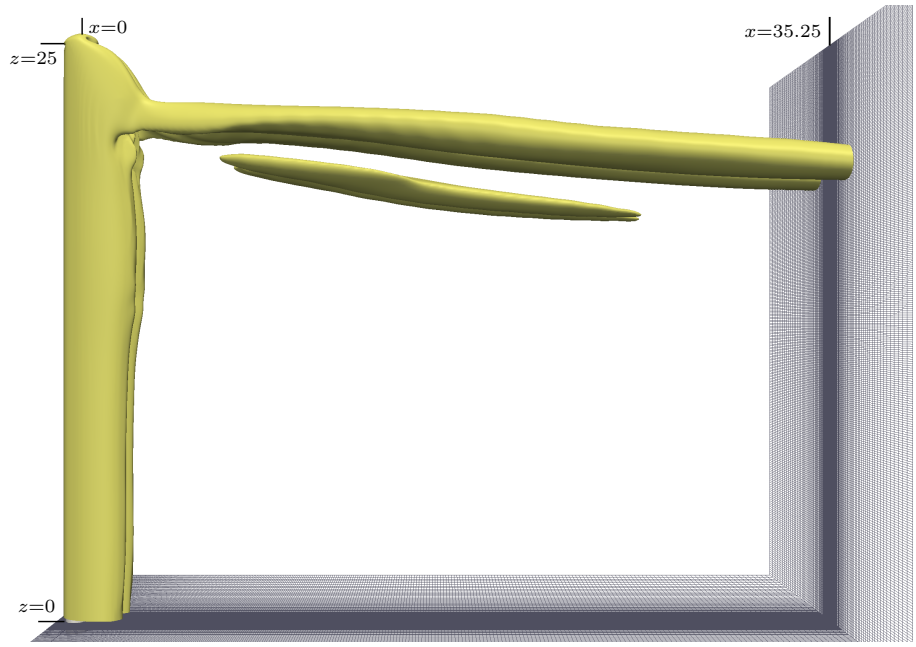

Figure 4.10: Isosurface of $\lambda_2 = -0.005$ for cylinder with two free ends and $^{L}/_{D} = 50$ showing a pair of trailing vortices emerging from a distance below the free end.

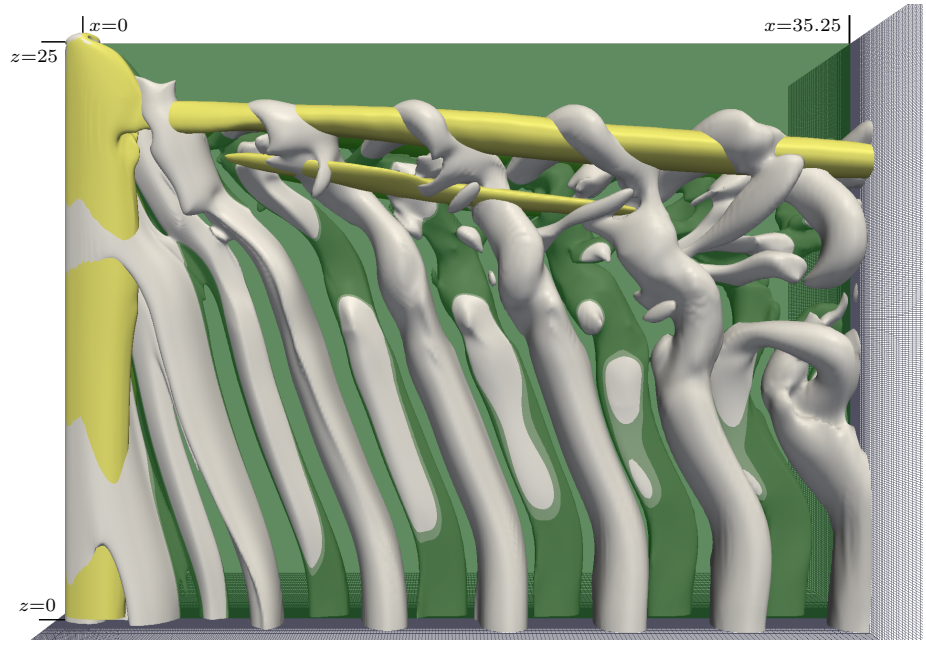

Figure 4.11: Isosurface of mean $\lambda_2 = -0.005$ (yellow) superimposed over an isosurface of instantaneous λ_2 (gray) for cylinder with two free ends and $^{L}/_{D} = 50$. Note that for consistency in the figure, a value of $\lambda_2 = -0.005$ is used for the isosurface of the instantaneous isosurface and not $\lambda_2 = -0.01$ which was used in previous figures of instantaneous λ_2.

Below the trailing vortices, another pair of streamwise vortices are identified by the λ_2-criterion with no apparent connection to any other vortices. Comparing with the instantaneous vortices in Figure 4.11, it is not certain what is causing these vortices, as no clear horizontal vortices can be seen in this region. Figure 4.12 show streamlines of the secondary flow, i.e. streamlines using v and w, in the $^{x}/_{D} = 12$ plane. Investigating these streamlines, the trailing vortices can be observed clearly inside the region predicted by the λ_2-criterion. No clear vortex can however be identified below the trailing vortices from the secondary flow streamlines. There is a region of streamwise vorticity where the λ_2-criterion identifies vortices, but from the secondary flow streamlines it appears to be more like a part of the trailing vortices than a separate pair of vortices. By investigating the secondary flow streamlines only, it is thus tempting to conclude that there is just one single pair of trailing vortices slightly larger than predicted by the λ_2-criterion and no separate pair of vortices below these.

The two methods used here for visualising the vortical structures in the mean wake give results that is to some extent contradicting. While the λ_2-criterion is a very specific and well tested criterion for identifying vortices, plotting streamlines

is closer to the basic physics of the flow. The results when using streamlines is however influenced by the choice of initial points and the number of streamlines which could lead to biased results. From the results in the present study it is neither certain whether a pair of streamwise vortices do exist under the trailing vortices, nor if the λ_2-criterion performs badly in this case. To give a certain answer to this, the case should be studied in more detail and other methods for identifying vortices should be tested.

Below the trailing vortices, near the bottom of Figure 4.12, another pair of vortices can be observed. Looking at the streamwise vorticity, these vortices are weak compared to the trailing vortices and when using $\lambda_2 = -0.005$ they were not identified using the λ_2-criterion. When using even lower values of λ_2 some structures appear in this region, but the results appear very noisy at this point and is not shown here. From the vertical position of these vortices they appear to be originating from the vortex dislocations, which are further discussed in Section 4.5. Since the vortex dislocations occur at a very low frequency, this corresponds well with the low mean streamwise vorticity.

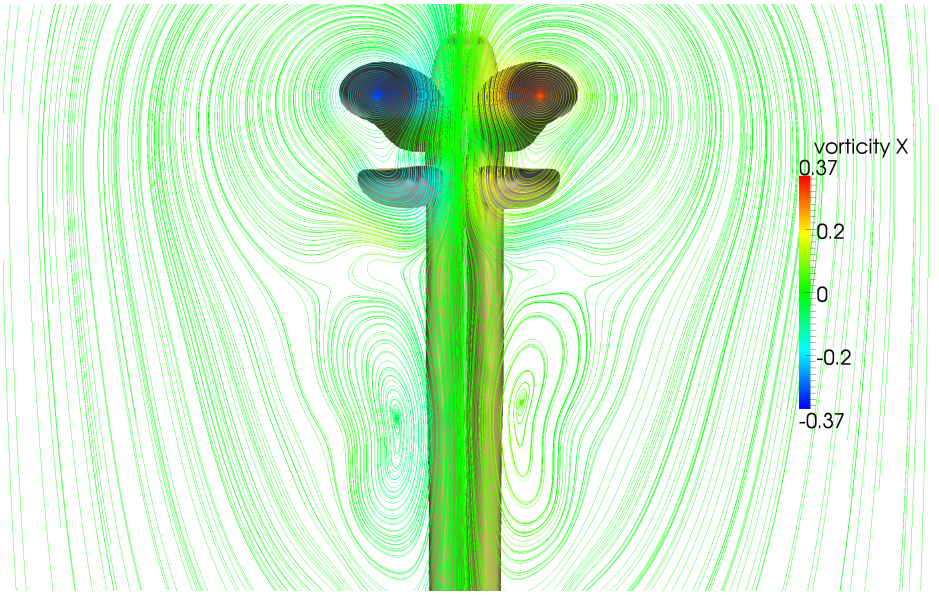

Figure 4.12: Isosurface of mean $\lambda_2 = -0.005$ shown behind secondary flow streamlines at $x/D = 12$.

Figure 4.13 shows the mean arch vortex, visualised by streamlines, which is symmetric about the $y = 0$ plane. Due to the periodic motion of the instantaneous arch vortex (shown in Figure 4.9), the vortex arms appear with an angle out from the cylinder.

Behind the cylinder and near the free end, a region of downwash occurs. This can be seen in Figure 4.14, which show contours of w in the $y = 0$ plane behind the

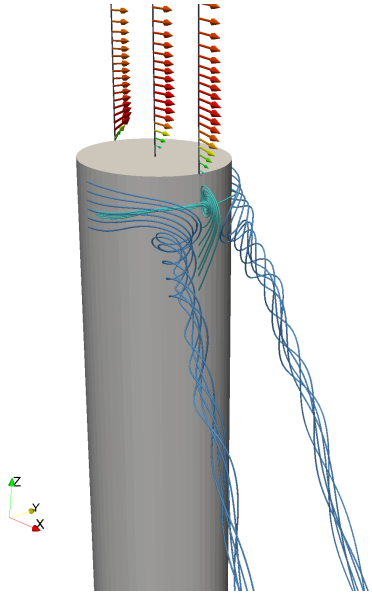

Figure 4.13: Mean arch vortex visualised by streamlines.

cylinder. The appearance and behaviour of the mean trailing vortices is believed to be heavily influenced by this downwash (see e.g. Krajnoviä [16]). Although not shown here, the horizontal part of the vortices shed from the end cell, and thus the mean trailing vortices, appear below the region with minimum w. From these observations it seems like the downwash behind the free end is causing the suppression of vortex shedding near the free end.

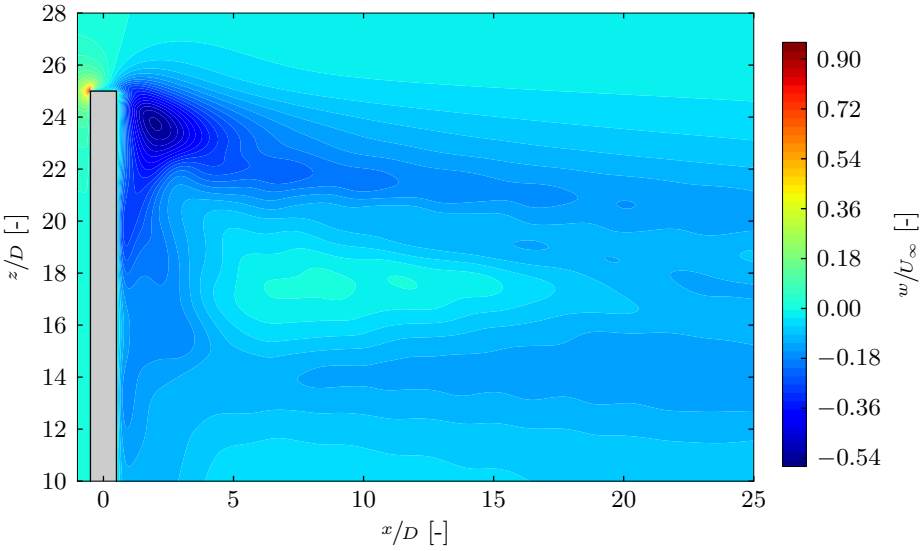

Figure 4.14: Contour plot of mean w in the $y = 0$ plane for a cylinder with two free ends and $^{L}/_{D} = 50$. Behind the free end, a downwash area can be observed.

4.5 Spanwise Variation of Wake Fluctuations

The method for estimating wake fluctuations as described in Section 2.2.2 was used on a $\tau = 8200$ long data set with several lines placed in the wake. The points were placed from $^{z}/_{D} = 0$ to $^{z}/_{D} = 26$ and with a spacing of $0.25D$.

Figure 4.15 shows a part of the time series obtained at a line placed in $(x, y) = (3D, 0.25D)$ for the four variables. This position in was chosen because it is close to the cylinder, approximately in the region where the vortices propagate downstream and should because of this capture the vortex shedding features well. The oblique vortex shedding is clearly shown as fluctuations in all four variables appearing bent to the right in the plots. All four plots also clearly show vortex dislocations appearing regularly at around $^{z}/_{D} \approx 15$. The dislocations can be seen most clearly in the plot of $^{u}/_{U_\infty}$ as regions of negative velocity and in the plot of $^{v}/_{U_\infty}$ as regions of velocities close to zero. In the plot of v one can also see that the vortex dislocations occur because the shedding angle in the region between $^{z}/_{D} = 15$ and $^{z}/_{D} = 20$ becomes so large that the vortex splits causing the low v-velocity region. As time advances the phase difference increases and for the fourth region of positive v-velocity counting from $\tau = 0$ at $^{z}/_{D} = 0$, the v-velocity above and below the dislocation is completely out of phase. After this point in time the phase difference decreases as the end cell vortices catch up with the central vortices in front which finally shed as a continuous spanwise vortex.

The detected frequency peaks for the four variables at $(x, y) = (3D, 0.25D)$ are shown in Figure 4.16. Each point is coloured by the corresponding power from the frequency spectrum. For the u- and w-signals, the dislocation frequency is clearly shown. It is however not detected in the v-signal even though some disturbance can be seen in the time sequence shown in Figure 4.15.

The central cell shedding frequency can be clearly observed starting at $^z/_D = 0$ and extending up to $^z/_D \approx 18$ in all four variables. This also applies for the end cell shedding frequency which is detected between $^z/_D \approx 12$ and $^z/_D \approx 22$. More exact estimates of the area influenced by the cells could be given, but depending on what powers are regarded as influencing, there are large uncertainties. It is for example likely that there is a peak at the end cell shedding frequency for $^z/_D < 12$ which has not been detected due to the choice of Δ (see Section 2.2.2). In the transitional area between the two vortex shedding cells, a frequency close to each of the cell frequencies has been detected. The lower one is a beat frequency lower than the end cell frequency and the higher one is a beat frequency higher than the central cell frequency. These occur due to interaction between the different fluctuations in this region.

In addition to the previously discussed frequencies, two higher frequencies are detected over a significant z-range in more than one of the variables. These frequencies are, as shown in Figure 4.16, denoted St_1 and St_2 in non-dimensionalised form. As seen in the 2D convergence study (see Table 3.3), the drag force on a cylinder fluctuates with a frequency twice the size of the vortex shedding frequency. This corresponds well with St_1 and St_2 which are found to be very close to twice the end cell frequency and the central central cell frequency respectively.

Table 4.1 summarises the findings discussed in the previous paragraphs and provide numerical values for the frequencies. Inoue and Sakuragi [11] and Williamson [31] measured the central and the end cell shedding frequencies and these are shown in comparison to the present results in Table 4.2. Williamson measured the shedding frequencies on cylinders with $^L/_D > 140$, but both he and Inoue and Sakuragi found very small variations in frequency when increasing the aspect ratio. The present results compare well with these results and is placed in between the previous findings.

Table 4.1: Summary of wake frequencies for cylinder with two ends. The estimates of spanwise extent are based on results presented in Figure 4.16.

Parameter	Value [-]	Connection	Spanwise extent
St_D	0.0232	$= \mathrm{St}_L - \mathrm{St}_e$	$^z/_D \in [10, 18]$
St_e	0.1341		$^z/_D \in [12, 22]$
St_L	0.1573		$^z/_D \in [0, 18]$
St_1	0.2683	$\approx 2\mathrm{St}_e$	$^z/_D \in [16, 21]$
St_2	0.3134	$\approx 2\mathrm{St}_L$	$^z/_D \in [0, 13]$

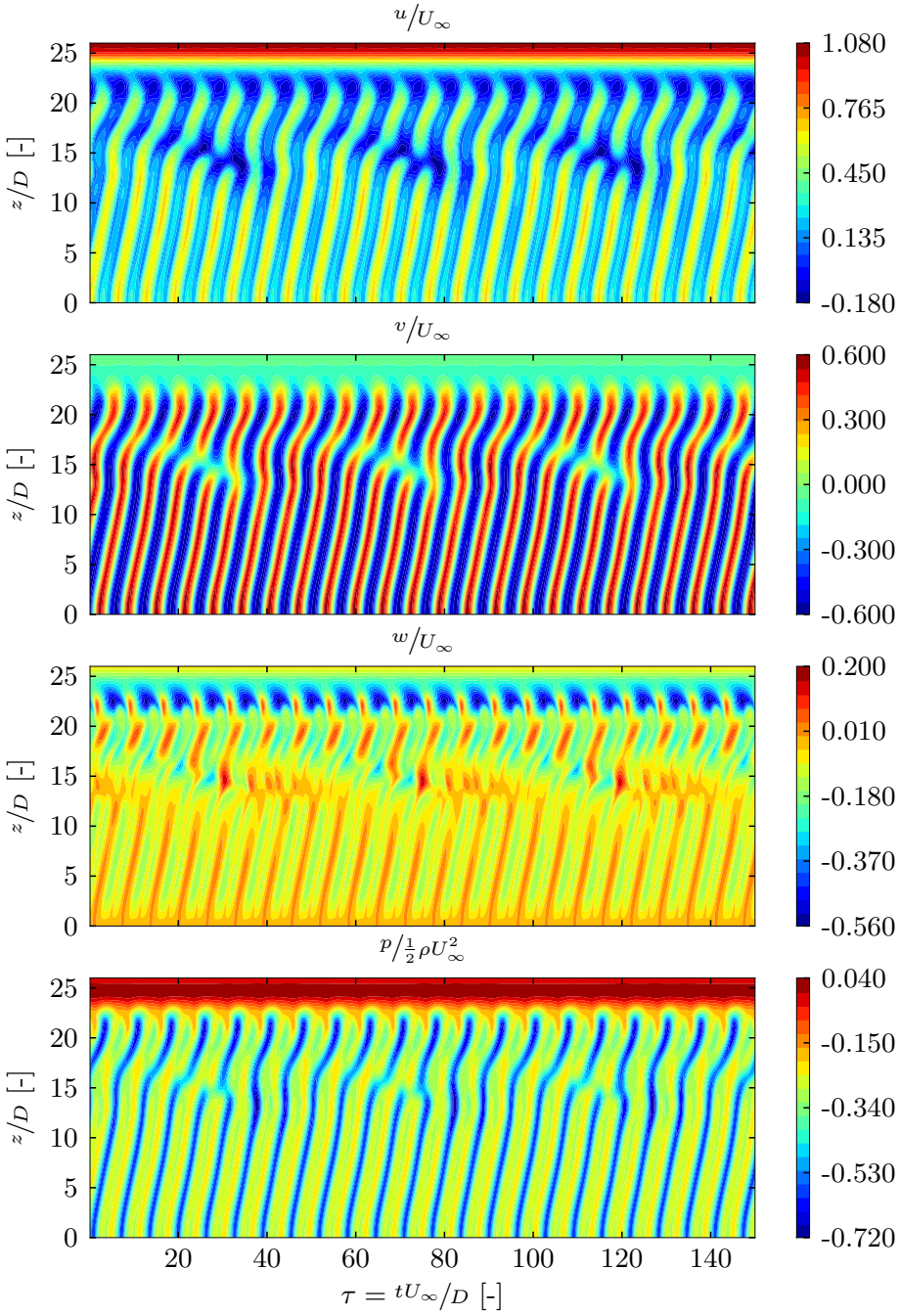

Figure 4.15: Time series, from the top down, of u, v, w and p at $(x, y) = (3, 0.25)$ and $z \in [0, 26]$.

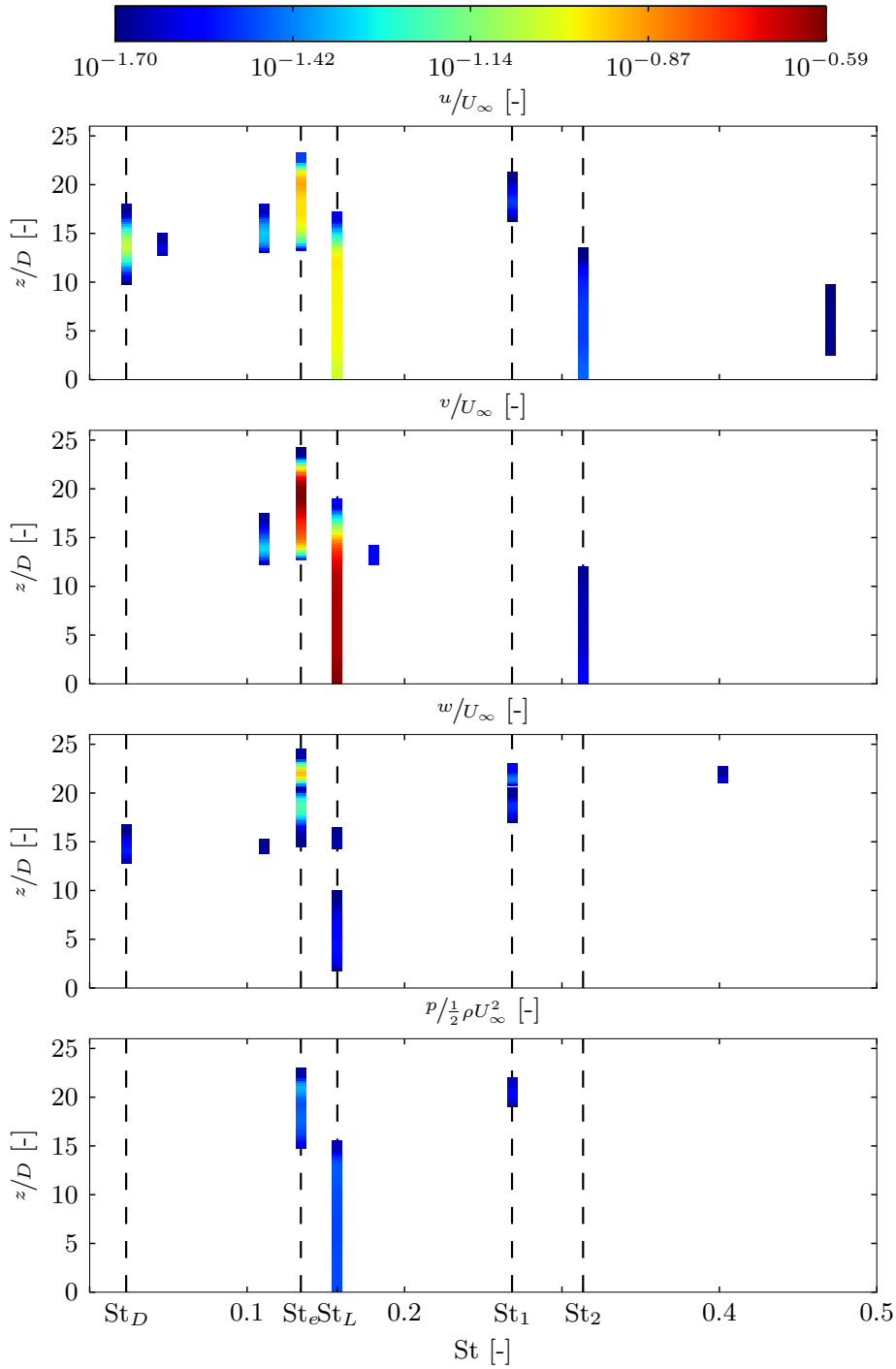

Figure 4.16: Detected frequency peaks in u, v, w and p. The detected points are coloured by the corresponding power.

Table 4.2: Comparison of central and end cell shedding frequencies from different studies. Values from other authors are approximate. The results from Williamson [31] are measured on cylinders with $^{L}/_{D} > 140$.

Author	Method	St_e [-]	St_L
Williamson [31]	Experimental	0.142	0.160
Inoue and Sakuragi [11]	CFD	0.128	0.150
Present study	CFD	0.1341	0.1573

The peaks shown in Figure 4.16 is, as previously discussed, detected algorithmically and the algorithm might not detect all the peaks. To verify the results, spectra at selected $^{z}/_{D}$ have been inspected manually. Figure 4.17 shows selected time series and spectra for v and contrary to Figure 4.16 there are two distinct peaks at $^{z}/_{D} = 24$ where the latter is a harmonic of the end cell shedding frequency. This peak has a relatively low power and are thus not detected as a peak even though it does appear as distinct in the frequency spectrum. The peaks appear so clearly because of the logarithmic scale in the frequency spectrum which the peak detection algorithm does not take into account. Incorporating a logarithmic scaling into the peak detection could improve the results, but this has not been considered in the present study. The same issue occur in the frequency spectrum at $^{z}/_{D} = 0$ where several harmonics of the central cell shedding frequency occurs, but only the two first peaks are detected. In the transition between the two cells, at $^{z}/_{D} = 15$, the algorithm performs well and detects the dislocation frequency, the two cell frequencies and just few of the less pronounced peaks.

Figure 4.18 shows parts of the time series and the frequency spectrum for u at $(x, y, z) = (3D, 0, 0)$. Again, several multiples of St_L can be observed whereas the peak detection algorithm only detected the first two. Additionally, a small peak can be seen at the dislocation frequency which also has not been detected by the algorithm. This means that, although with small influence, the vortex dislocations can be detected in the wake at the centre of the cylinder span for $^{L}/_{D} = 50$.

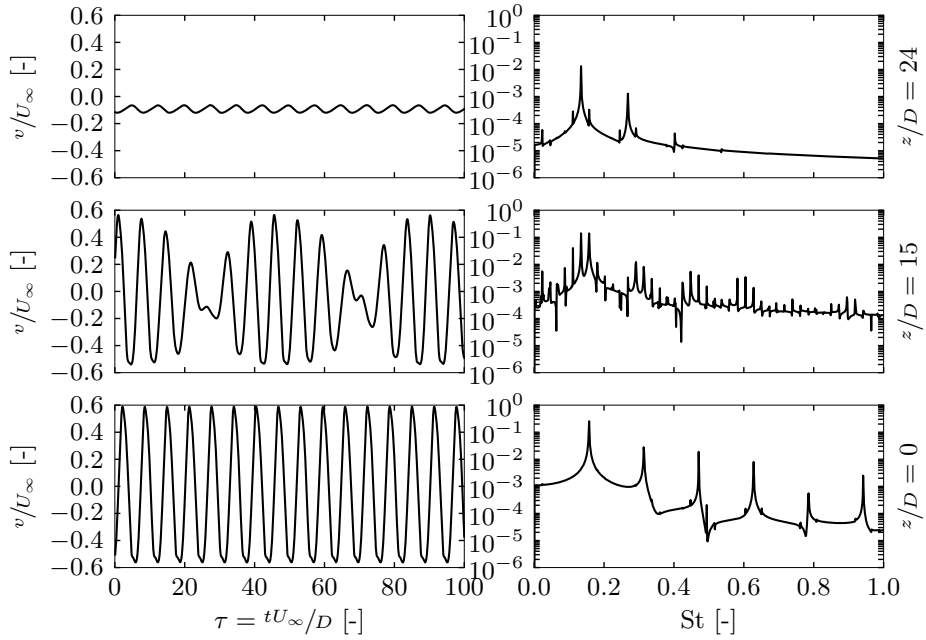

Figure 4.17: Time series and frequency spectra for v at $(x, y) = (3D, 0.25D)$ for selected ${}^{z}/_{D}$.

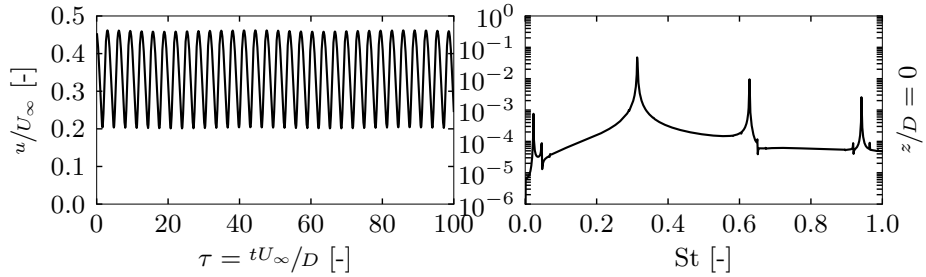

Figure 4.18: Time series and frequency spectrum for u at $(x, y, z) = (3D, 0, 0)$.

4.6 Oblique Vortex Shedding Angle

As previously discussed, the vortices are shed from the cylinder with an oblique angle. This affects the shedding frequency compared to a 2D or an infinite cylinder, where vortices are shed parallel to the cylinder at $\mathrm{Re} = 100$. Williamson [31] gives a transformation between the oblique shedding frequency and the parallel shedding

frequency as a function of the oblique shedding angle, θ (repeated from Section 1.1):

$$\mathrm{St}_0 = \frac{\mathrm{St}_\theta}{\cos(\theta)}, \tag{4.1}$$

To compare the 2D parallel shedding frequency to the oblique shedding frequency, the θ angle has to be found. This is done by investigating the scalar field of v in the xz-plane at $y = 0$ at the same time instant as used in Figure 4.1. As shown in Figure 4.19, the oblique vortices can be observed clearly as areas of positive and negative v. The black line in Figure 4.19 marks a line of constant $v = 0$. Although this line does not represent a vortex core, which is offset to one of the sides in y-direction, it should correspond well to the slope of the vortex. For this analysis, the oblique part of the central cell is of interest and this region is marked by two crosses in Figure 4.19. Between the two crosses, the line is not completely straight so linear regression is used and theta is found by

$$\theta = \frac{\pi}{2} - \arctan(-a), \tag{4.2}$$

where a is the slope of the regression line. The regression line is shown in Figure 4.20 and in the present case, the shedding angle was found to be $\theta \approx 19°$. For comparison, Williamson [31] reports an angle $\theta \approx 12°$ at Re $= 100$. The cylinders used by Williamson were of different aspect ratios, all longer than $L/D = 100$, and all giving approximately the same shedding angles. Comparing with the present result, it appears that the shedding angle starts to increase when the aspect ratio is reduced towards $L/D = 50$.

Table 4.3 compares the transformed central cell shedding frequency (St_{L0}) with the 2D shedding frequency. The transformed central cell shedding frequency is 2.3 % below the 2D frequency which is fairly close.

Table 4.3: Transformation to parallel shedding frequencies

Case	Variable	Value [-]
2D	St	0.1700
$L/D = 50$	St_L	0.1573
$L/D = 50$ (transformed)	St_{L0}	0.1661

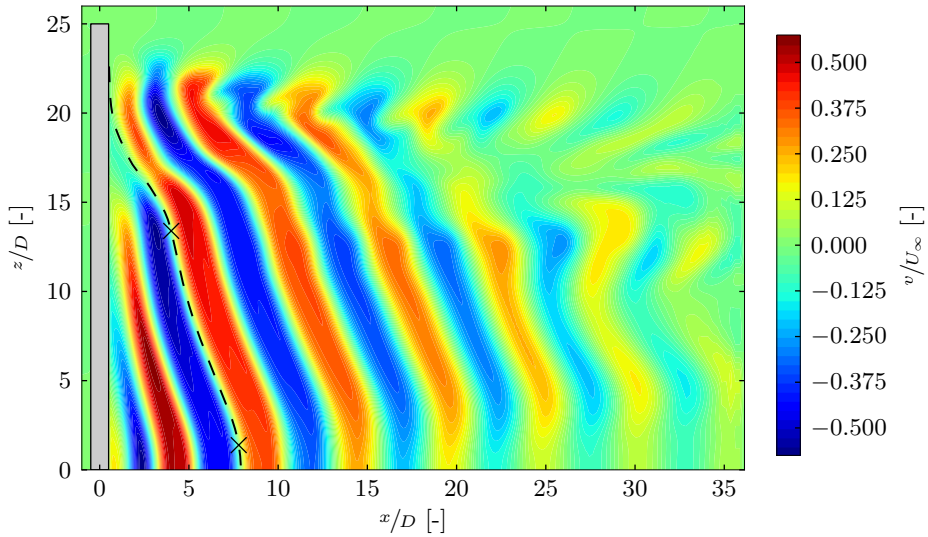

Figure 4.19: Contour of v in xz-plane at $y = 0$.

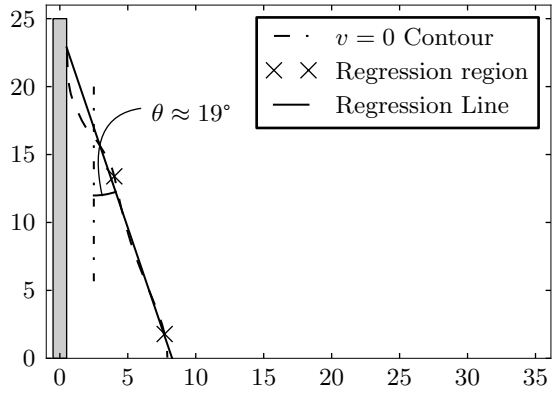

Figure 4.20: Regression line for determining vortex shedding angle θ.

4.7 Lift and Drag Forces

Compared with results from Kravchenko et al. [17], Inoue and Sakuragi [11] report slightly lower C_L and C_D for a $^L/_D = 50$ cylinder than for a 2D cylinder at Re = 100. Liu et al. [18] simulated a truncated cylinder with $^L/_D = 10$ at $100 \leq \text{Re} \leq 200$ and found that the cross-sectional lift coefficient decreases near the free end.

Table 4.4 compares the lift and drag coefficients obtained in the grid dependence study (see Section 3.2) with data from the finite cylinder. As expected, the drag

coefficient is lower for the finite cylinder case, in this case with 6 %. The lift coefficient on the other hand, is less than a tenth of the 2D lift coefficient. It seems very unlikely that the end cell alone has this big an influence on the lift coefficient, especially when the drag coefficient still is the same order of magnitude as for the 2D case. The introduction of a free end does however, as discussed in Section 4.6, also introduce oblique vortex shedding in the central cell. Due to this obliqueness, the vortex shedding is in different phases at different parts of the cylinder. Since the lift force mainly is a result of the pressure distribution caused by the vortex shedding, this means the cross-sectional lift force will also be in different phases along the span. Globally, this will result in cancelation effects and thus a reduction in the lift force.

Table 4.4: Comparison of lift and drag coefficients for 2D cylinder and finite cylinder with two free ends and $^{L}/_{D} = 50$.

Case	$^{L}/_{D}$ [-]	C_L	C_D	$C_{D,amp}$
Present study, 2D	-	0.3056	1.3600	0.0084
Present study	50	0.0294	1.2766	0.0052
Inoue and Sakuragi [11]	50	0.2320	1.0020	0.0060

Investigating the frequency spectrum for the lift force, which is shown in Figure 4.21, one can observe peaks for the cell shedding frequencies St_L and St_e as found in Section 4.5. Although the central shedding cell is the larger of the two cells in spanwise extent, the peak with the highest power is at the end cell frequency. Again, this is due to the cancelation effects in the central cell reducing its influence on the lift force. In addition to the two cell frequencies another frequency peak, stronger than the central cell frequency, occurs at $\mathrm{St}_L + \mathrm{St}_D$. Looking back to the wake fluctuations detected in Figure 4.16, there is only a small peak detected at this frequency in the transition between the two shedding cells. While it seems implausible that a wake fluctuation with such short spanwise extent and low power has a large impact on the lift force, this frequency has not been detected anywhere else in the wake. Thus, the available data indicate that this contribution to the lift force origins from the transitional region between the two cells.

Contrary to the drag force on a 2D cylinder, the drag force on the finite cylinder with two free ends is not dominated by fluctuations twice the vortex shedding frequency. As shown from the frequency spectrum in Figure 4.22, the fluctuating part of the drag force is dominated by the dislocation frequency and two of its harmonics. As demonstrated in Chapter 3, the drag force fluctuations are periodic with twice the vortex shedding frequency. The fluctuations of twice the cell shedding frequencies appear in the frequency spectrum, but are weak compared to the dislocation frequency. While the vortex dislocations appear to influence the drag force fluctuations in a strong manner, it should be noted that the fluctuations in drag force itself is minor compared to constant drag force. For the cylinder with two free ends, the drag force amplitude is just 0.4 % of the mean

drag force and thus a minor contribution to the total drag force.

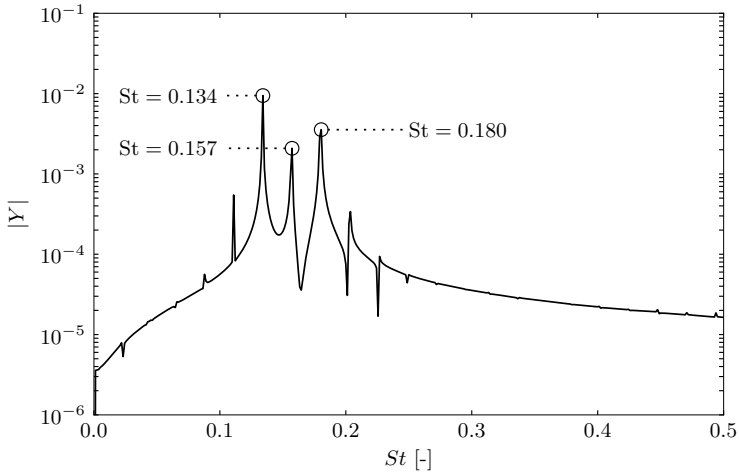

Figure 4.21: Frequency Spectrum of the lift force on a finite cylinder with two free ends and $^{L}/_{D} = 50$.

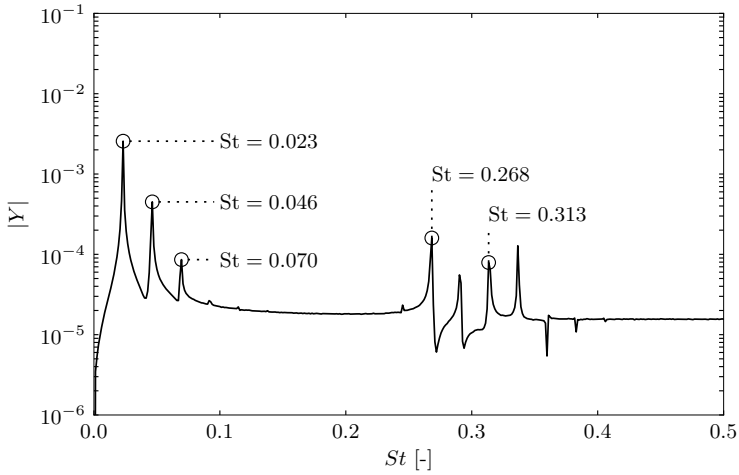

Figure 4.22: Frequency Spectrum of the fluctuating part of the drag force on a finite cylinder with two free ends and $^{L}/_{D} = 50$.

4.8 Practical Considerations

There are several different offshore constructions which could be modelled as a finite cylinder, for example parts of a subsea foundation in current. Another example is a spar platform where the Reynolds number will be very large due to the large diameter. The results from the present study are for a low Reynolds number which mostly do not occur in practical engineering situations. As previously discussed however, the present results share many similarities with results published for higher Re. On this basis, the following section will discuss some practical considerations with emphasis on the flow around the free end of a cylinder.

The most obvious similarity between the present low Re simulation and published results of large Re cases is the existence of a pair of trailing vortices behind the free end. It is tempting to draw parallels between these trailing vortices and the trailing vortices behind the wingtips of an airplane. The wingtip vortices of an airplane causes lift-induced drag and can be a hazard for smaller airplanes coming behind (Wikipedia [30]). On modern airplanes, it is common to fit the wings with an wingtip device, commonly called a winglet, to reduce the size of the wingtip vortex (see Figure 4.23 for an example).

Figure 4.23: Example of a winglet on an airplane. From Wikipedia [30].

Fitting a finite cylinder with similar devices could reduce the strength of the trailing vortices. One possibility is to add a disk of a larger diameter, say for example $2D$, on the top of the cylinder and investigate whether this will have a similar effect as a winglet. This has the advantage of that it is direction independent and does not have to adjusted if the inflow direction changes. It should, of course, be noted that it is not known whether such a device will have the desired effect and is merely a theory. Other possibilities include trimming the free end in various ways, for example by bevelling the edges. This was experimentally investigated by Park and Lee [22] which found that the downwash reduced due to the trimmed ends they tested.

It is however not given that it is desirable to reduce the strength of the trailing vortices. Although no direct comparisons have been made, the trailing vortices behind a finite cylinder does not appear to be as strong. While they may have adverse effects on other structures close to the finite cylinder, for example a mooring line, it is observed that the trailing vortices suppress the von Karman vortex shedding. Based on this observation it is theorised that increasing the trailing vortices' strength could suppress even more of the vortex shedding. Since it seems like there is a connection between the downwash behind the cylinder and the trailing vortices, a possibility is to design a device that increases the downwash behind the cylinder. With the cost of increased drag, one could for example mount a plate or foil above the cylinder free end with an angle as shown in Figure 4.24. Again, this sort of device has not been simulated so it is not certain whether it will have the effect that it is wished for.

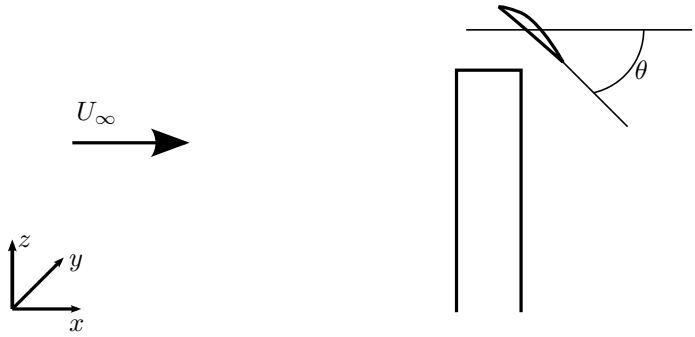

Figure 4.24: Potential device for increasing downwash behind the free end.

Chapter 5

Results and Discussion: Wall Mounted Cylinder

The results presented here were obtained by simulating a wall mounted cylinder with a free end with as described in Section 3.3. From the initial conditions, the simulation was first run until it reached a steady state. After reaching a steady state, the simulation were run for several shedding periods to obtain the time series and statistics used in this chapter.

Due to issues compiling parts of the post processing utilities on the Ve supercomputer (previous simulations were run on Njord), the λ_2 scalar field was not successfully computed for this case. As an alternative for identifying vortices, the aboslute value of the vorticity is used for analysis of the instantaneous flow field and streamwise vorticity is used for the mean flow.

5.1 Boundary Layer

The boundary layer thickness is an important parameter affecting the flow near the wall. At low Re_x, which is the Reynolds number based on the flow distance across the wall, the boundary layer is laminar and Blasus' formula for the boundary layer thickness (δ) applies (see e.g. White [29]):

$$\delta(x) = \left(\frac{\nu x}{U_\infty}\right)^{1/2}, \tag{5.1}$$

or non-dimensionalised using the cylinder diameter:

$$\frac{\delta(x)}{D} = \left(\frac{1}{\mathrm{Re}_D} \cdot \frac{x}{D}\right)^{1/2}, \tag{5.2}$$

where, for clarity, the Reynolds number based on the cylinder is denoted Re_D. Using the distance from the domain inlet to the cylinder centre, this gives a theoretical, undisturbed boundary layer thickness of $\delta/D = 0.41$ at the cylinder centre.

For comparison, the mean u velocity is measured as a function of z at $y/D = 8$ and for different x. At this y-distance from the cylinder the influence from the cylinder is limited so results should be comparable to the Blasius boundary layer. As shown in Figure 5.1 however, the boundary layer is much thicker than what predicted above. The horizontal velocity also precedes U_∞ at certain z in all the velocity profiles shown, contrary to what laminar boundary layer theory shows. For the velocity profiles at $x/D = -4$ and $x/D = 0$ some overshooting of U_∞ are to be expected because the cylinder will block the flow and thus increase the streamwise velocities in its vicinity.

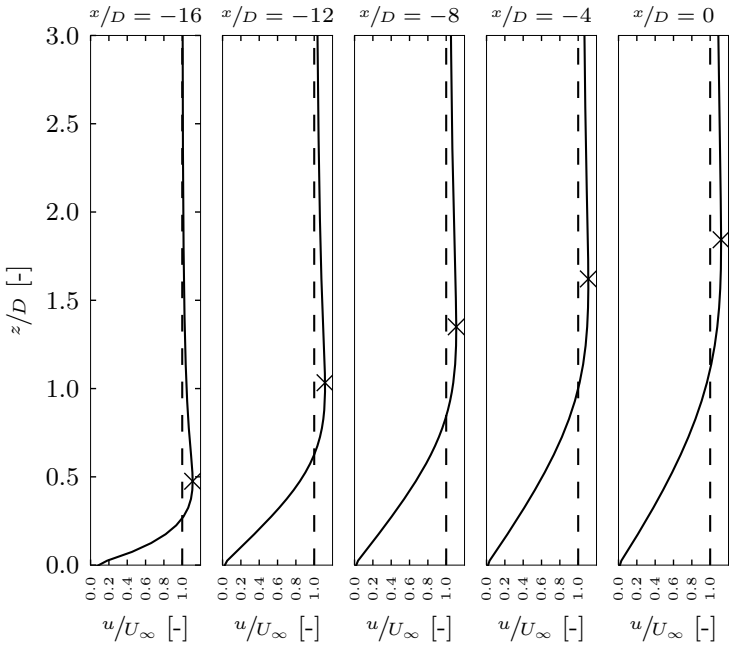

Figure 5.1: Boundary Layer evolution over wall. The samples are taken at $y/D = 8$ and show the boundary layer overshooting U_∞. The crosses mark the position of each velocity profile's maximum.

The reason for this poor consistency is believed to be due to the grid resolution in the boundary layer (personal communication, Gallardo Canabes [9]). When the

boundary layer artificially overshoots U_∞ in the far upstream end, this appears to let the boundary layer grow unrealistically large downstream.

Due to these issues, an estimate of the numerical boundary layer thickness is not given. Several authors have suggested that the boundary layer thickness have limited effect on the horseshoe vortex system forming near the wall-cylinder junction (see Simpson [27]), but the data is sparse. It is thus believed that the results from this simulation are realistic to some extent, but the results should be interpreted with these findings in mind.

5.2 Vortex Shedding Pattern

Figure 5.2 shows the isosurface of $|\boldsymbol{\omega}^{U_\infty}/_D| = 0.15$ at a time instant. As for the cylinder with two free ends, the vortices bend horizontally and through the $y = 0$ plane and connect to a vortex of opposite rotation near the free end. Just below these horizontal vortices, the vortices are shed in an oblique pattern. This region is however dominated by the transition between the end cell and the central cell, and appears chaotic. Further down in the spanwise direction, a region of parallel vortex shedding occurs before the vortices once again are shed in an oblique manner when approaching the wall. Vortices shed from the cylinder close to the wall are bent horizontally through the $y = 0$ plane and join vortices of opposite rotation, similar to the behaviour of the vortices near the free end. A detailed view of this is shown in Figure 5.3.

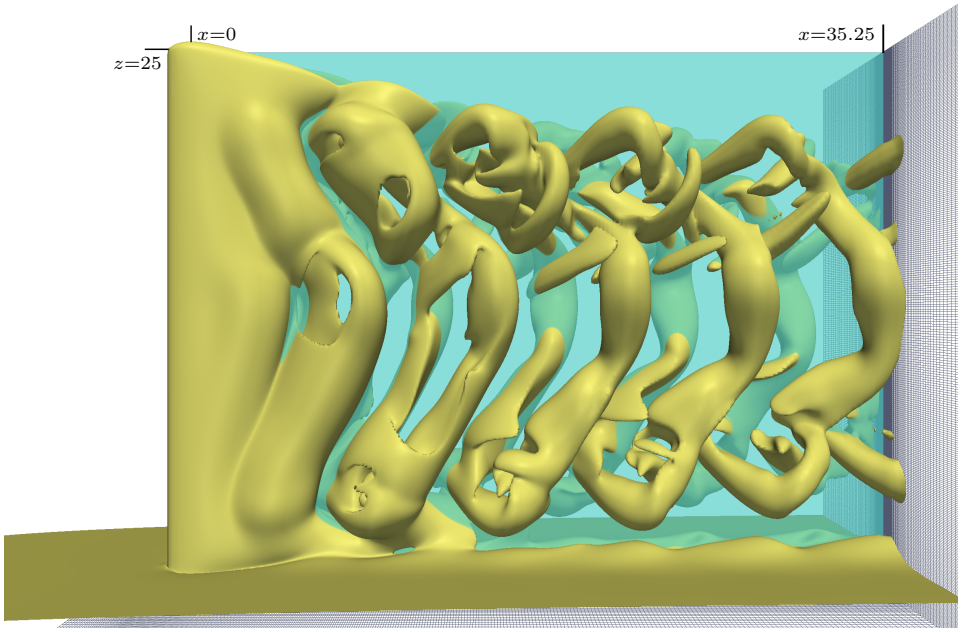

Figure 5.2: Isosurface of $|\boldsymbol{\omega}^{U_\infty/D}| = 0.25$ for wall mounted cylinder with ${}^{L}/_{D} = 25$. The semitransparent cyan plane is located at $y = 0$ to give an indication of the vortex location in y-direction. U_∞ flows along positive x-axis and the no-slip boundary ($z = 0$) is at the bottom of the figure.

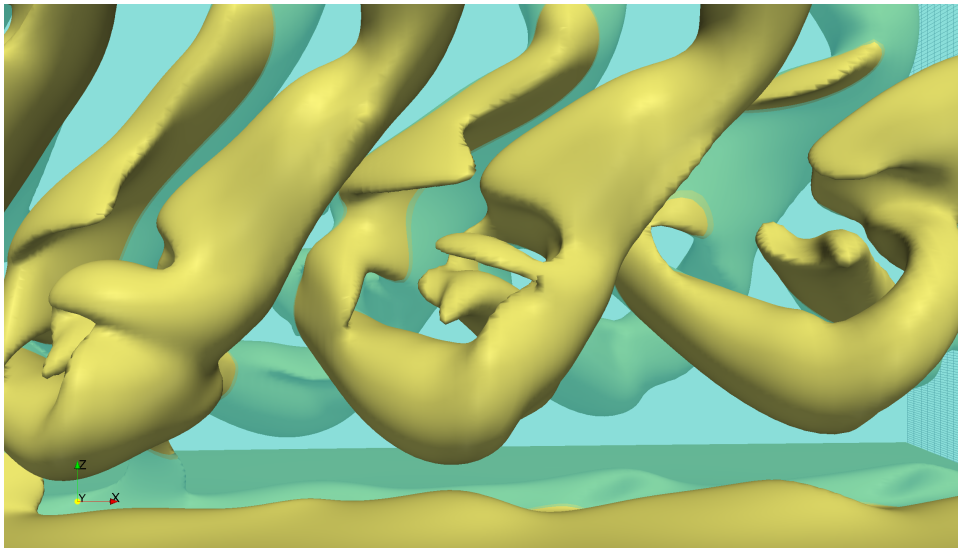

Figure 5.3: Detail view of vortex connections near wall using an isosurface of $|\boldsymbol{\omega}^{U_\infty/D}| = 0.15$. The semitransparent cyan plane is located at $y = 0$ to give an indication of the vortex location in y-direction.

5.3 Mean Flow Field

To visualise the mean trailing vortices for the wall mounted cylinder, isosurfaces of $\omega_x {}^{U_\infty}/_D = \pm 0.25$ are shown in Figure 5.4. As for the cylinder with two free ends, a pair of trailing vortices can be observed near the free end. A pair of similar trailing vortices can be observed from the wall-cylinder junction, however these appear to be weaker since the isosurfaces terminate further upstream than those from the free end. The colouring of the positive and negative ω_x isosurfaces also shows that the free end trailing vortex on the negative y side (in front of the figure) has opposite rotation to the trailing vortex from wall-cylinder junction.

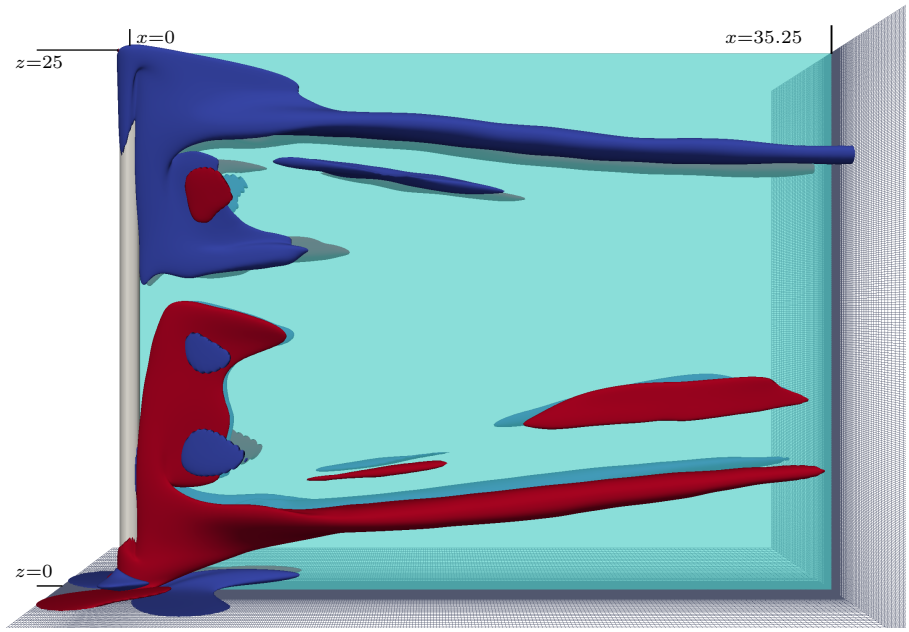

Figure 5.4: Isosurface of mean $\omega_x = \pm 0.15$ for wall mounted cylinder with ${}^L/_D = 25$.

The horseshoe vortex system forming near a wall-cylinder junction consists of one or several separate vortices forming in front of the cylinder, wrapping around and into the wake (see e.g. Baker [1]). At Re = 100, Figure 5.5 shows only a single vortex forming in front of the cylinders. This vortex propagates downstream and up in the wake as shown by the secondary flow streamlines in Figure 5.6.

Figure 5.6 also shows streamlines emitted in front of the cylinder. These streamlines wrap around both the cylinder and the horseshoe vortex before moving up in an upwash region right behind the cylinder. Although not as strong as the downwash region behind the free end, the upwash region seem to have a similar effect on the vortex shedding which are suppressed near the free end.

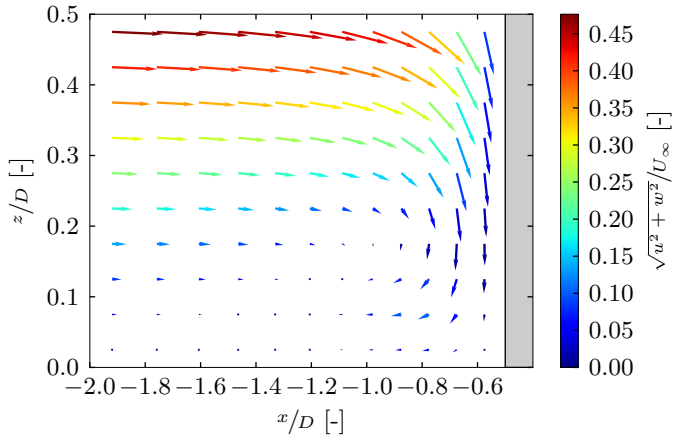

Figure 5.5: Velocity vectors in $y = 0$ plane showing a small vortex in front of the wall-cylinder junction.

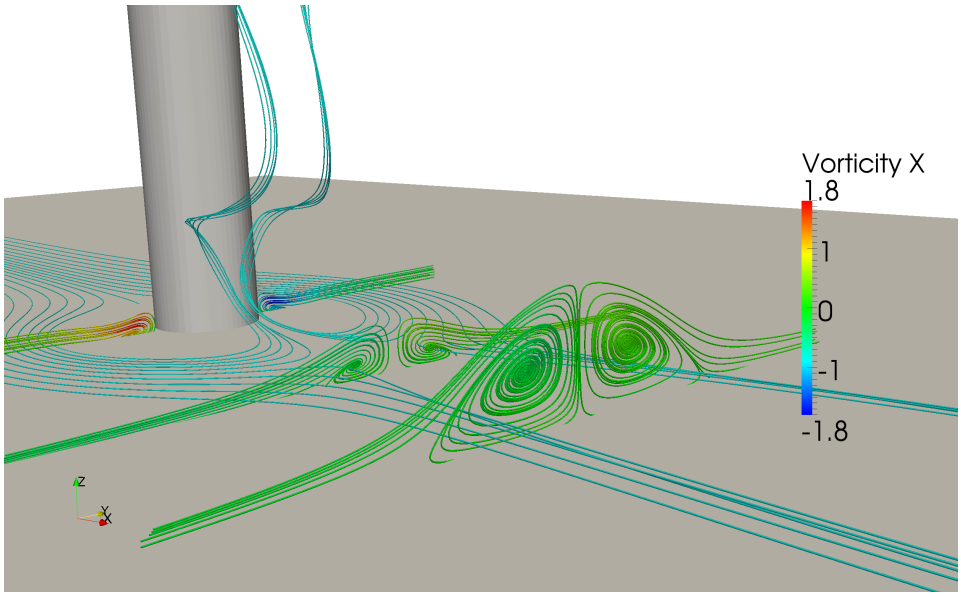

Figure 5.6: Mean horseshoe vortex visualised by secondary flow streamlines. The secondary flow streamlines are coloured by streamwise vorticity and emitted at $x/D = [0, 3, 5]$. Cyan streamlines are emitted from $x/D = -2$ right above the wall boundary and show an upwash region in the near wake.

5.4 Spanwise Variation of Wake Fluctuations

As for the cylinder with two free ends, the method described in Section 2.2.2 was used to analyse the wake fluctuations from lines of points placed in the wake. The data set used for the wall mounted cylinder was $\tau = 108\,000$ long and u, v, w and p were recorded at each point.

A part of the time series for the four variables recorded at a line placed in $(x, y) = (3D, 0.25D)$ is shown in Figure 5.7. Similar to the cylinder with two free ends (see Figure 4.15 in the previous chapter), the vortex dislocations between the end cell and the central cell can be observed clearly in the plots for u and v at around $^{x}/_{D} \approx 15$. From observing the vortices between the dislocations it can be seen that this is the region with parallel vortex shedding discussed in Section 5.2. For the wall mounted cylinder the vortex dislocations appear for a longer time than for the cylinder with two free ends, which means that the dislocation frequency must be lower. In the time history of w, a region of periodically large negative flow appears near the free end and a region of large positive flow appears near the wall. These are the horizontally bent vortices which were found near the cylinder ends in Section 5.2.

Figure 5.8 shows the frequency peaks detected from the time series. Due to the no-slip condition at $^{z}/_{D} = 0$, the vortex shedding does not occur until some diameters above the wall. Compared to the cylinder with two free ends (see Figure **??** in the previous chapter), the harmonic frequencies St_1 and St_2 appear less pronounced and the spanwise extent of the dislocation frequency (St_D) is smaller.

Contrary to the free end vortex shedding, the vortices near the wall do not shed in a separate cell and thus, no vortex dislocations occur near the wall. As observed in Section 5.2, the wall boundary does however cause oblique vortex shedding as this can be observed both above and below the region with parallel shedding in Figure 5.2. This implies that relative to a free end, the wall-cylinder boundary is weaker and influences the wake structure to a lesser extent.

The change in boundary condition at the bottom of the domain has also altered the vortex shedding frequencies, which are shown in Table 5.1. Compared to the cylinder with two free ends (see Table 4.1 in the previous chapter), the end cell shedding frequency of the wall mounted cylinder has been reduced with only 0.8 % which means that it is essentially unaffected by the introduction of the wall boundary condition. The central cell shedding frequency has been affected by the change is reduced by approximately 6 %. Due to the change in the central cell shedding frequency, the dislocation frequency is reduced accordingly.

It should be noted that while these results show that changing the boundary condition from a symmetry condition to a wall condition affects the flow behaviour in the wake, the physical interpretation of this change as following: Firstly, the cylinder aspect ratio is reduced from $^{L}/_{D} = 50$ to $^{L}/_{D} = 25$ and secondly, one of cylinder ends is mounted to a wall. Ideally, a third case with two free ends and

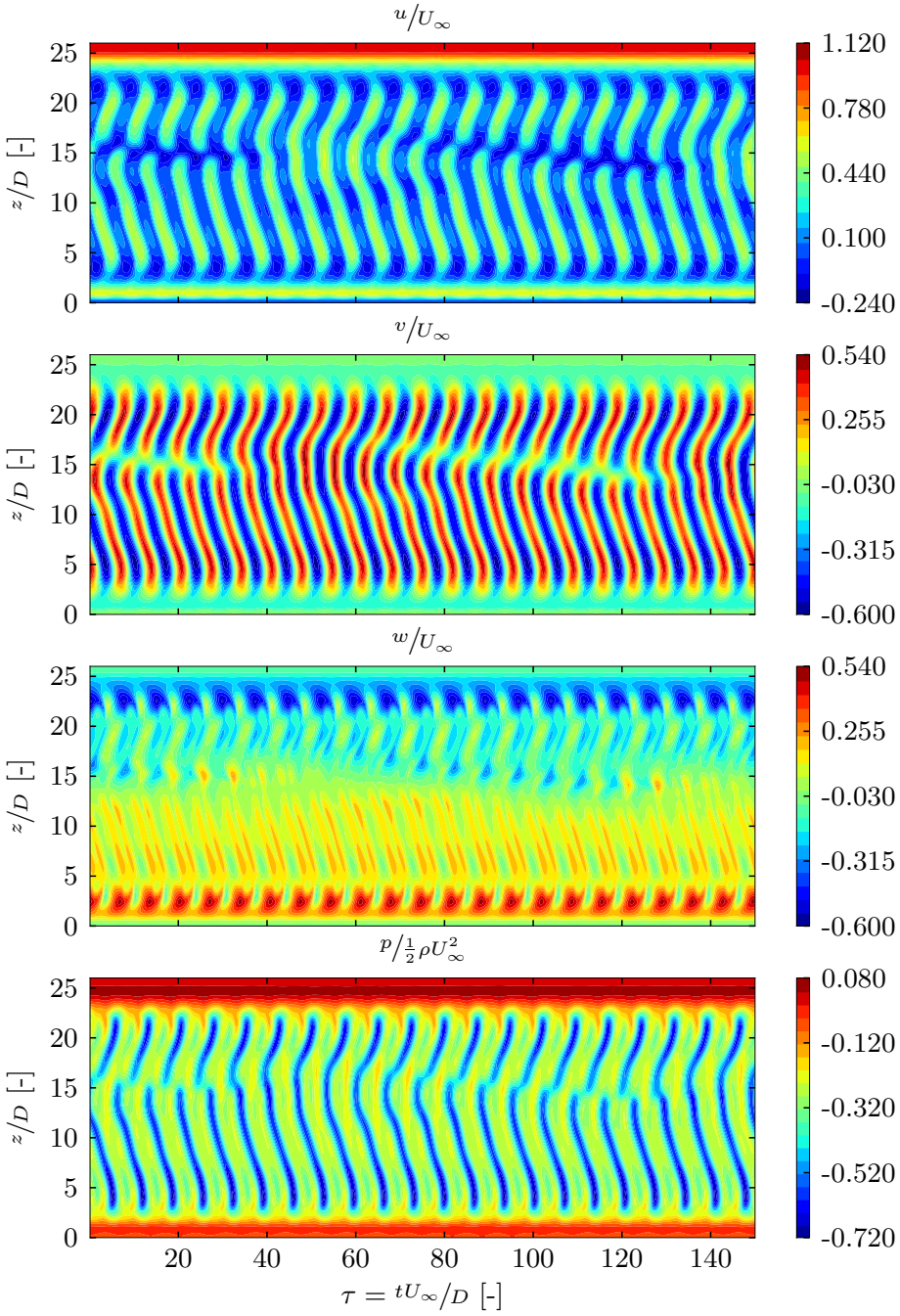

Figure 5.7: Time series, from the top down, of u, v, w and p at $(x, y) = (3D, 0.25D)$ and $z \in [0, 26]$ for wall mounted cylinder with $L/D = 25$.

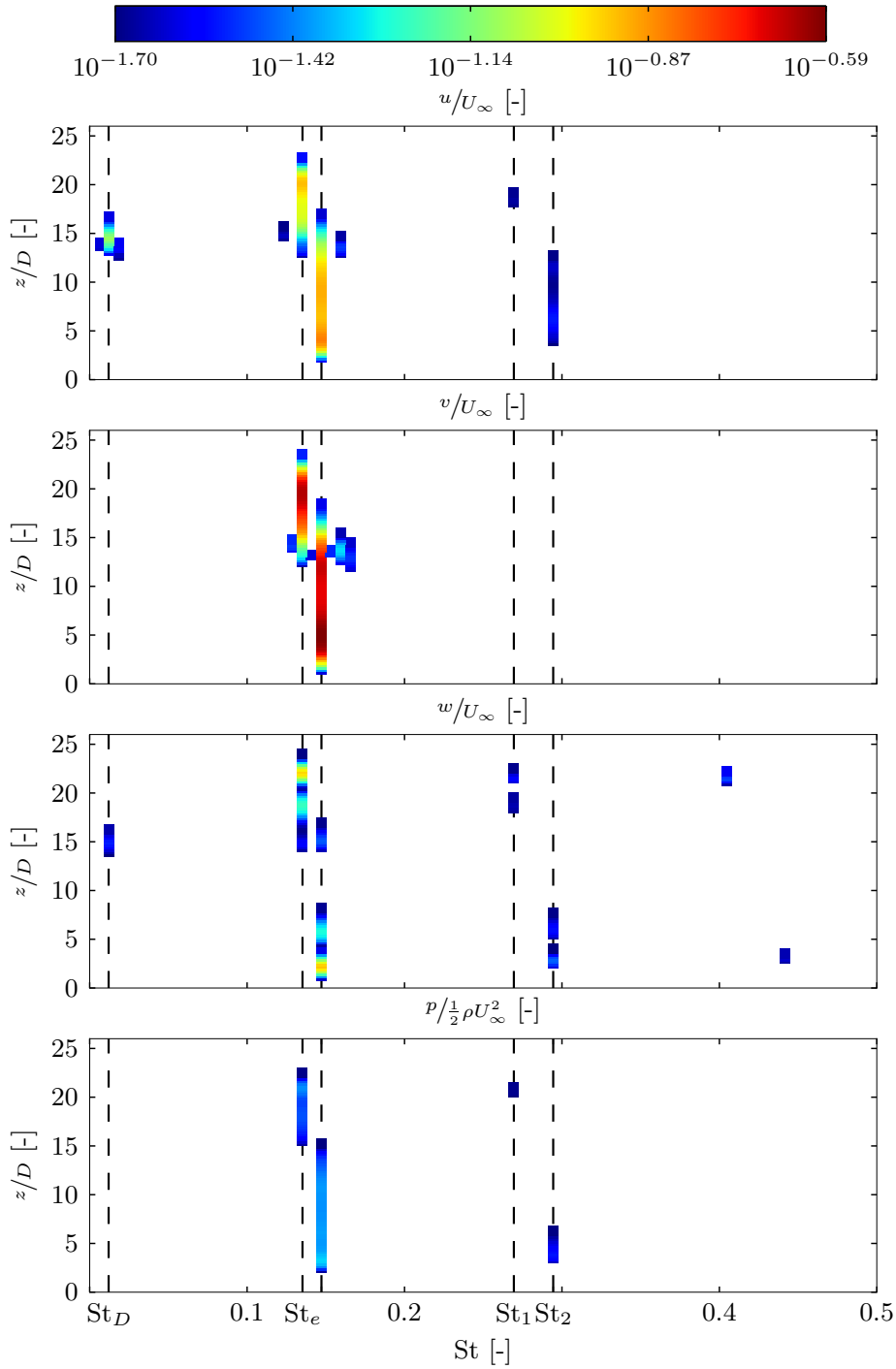

Figure 5.8: Detected frequency peaks in u, v, w and p for wall mounted cylinder with $^L/_D = 25$. The detected points are coloured by the corresponding power. The dashed line to the right of St_e marks St_L, but the label is omitted due to space limitations.

Table 5.1: Summary of wake frequencies for wall mounted cylinder. The estimates of spanwise extent are based on results from Figure 5.8.

Parameter	Value [-]	Connection	Spanwise extent
St_D	0.0120	$= St_L - St_e$	$z/D \in [13, 17]$
St_e	0.1352		$z/D \in [12, 23]$
St_L	0.1472		$z/D \in [1, 18]$
St_1	0.2694	$\approx 2St_e$	$z/D \in [18, 22]$
St_2	0.2944	$\approx 2St_L$	$z/D \in [2, 12]$

$L/D = 25$ should also have been simulated, but this has not been possible due to time constraints. Inoue and Sakuragi [11] do however give results for both an $L/D = 50$ and an $L/D = 25$ cylinder with two free ends. Table 5.2 compares these results to the two cases in the present study. In both cases the end cell shedding frequency remains approximately the same for both configurations. With Inoue and Sakuragi's data, a 3 % reduction in central cell shedding frequency is found when going from an $L/D = 50$ to and $L/D = 25$ cylinder. Using data of the present study a reduction of 6.4 % is found between a $L/D = 50$ cylinder with two free ends and a wall mounted cylinder with $L/D = 25$. This indicates that the central cell shedding frequency is reduced due to the reduction of aspect ratio as well as the introduction of a wall boundary condition at its base.

Table 5.2: Comparison of cell vortex shedding frequencies between present study and Inoue and Sakuragi [11]. The values from Inoue and Sakuragi are approximate values read from a graph.

Source	Configuration	L/D [-]	St_e [-]	St_L [-]
Present study	Two free ends	50	0.1341	0.1573
	Wall mounted	25	0.1352	0.1472
Inoue and Sakuragi [11]	Two free ends	50	0.128	0.150
	Two free ends	25	0.128	0.145

5.5 Lift and Drag Forces

No data on lift and drag forces have been found published for a wall mounted cylinder with $L/D = 25$ at $Re = 100$, so these results can only be compared with the other simulations in the present study. Table 5.3 shows the lift and drag coefficient from the 2D simulation as well as the two finite cylinders. The effect of the wall condition on the drag and the drag amplitude is small compared to the cylinder with two free ends. This small reduction is due to the suppression of vortex shedding near the wall-cylinder junction which leads to higher pressure behind the cylinder. Compared to the 2D cylinder, both finite cylinders have a smaller drag coefficient and this has been discussed in Section 4.7.

The lift coefficient for the wall mounted cylinder is larger than for the one with two free ends, but smaller than for the 2D cylinder. As for the cylinder with two free ends, the obliqueness of the vortex shedding causes cancelation effects as discussed in Section 4.7. The increase in lift compared to the cylinder with two free ends is explained by the increased spanwise region with parallel vortex shedding seen for the wall mounted cylinder.

Table 5.3: Comparison of lift and drag coefficients for the 2D cylinder and two finite cylinders simulated.

Configuration	L/D [-]	C_L	C_D	$C_{D,amp}$
2D	-	0.3056	1.3600	0.0084
Two free ends	50	0.0294	1.2766	0.0052
Wall mounted	25	0.0450	1.2639	0.0060

Figure 5.9 shows the lift force frequency spectrum which, similar to the lift force spectrum for the cylinder with two free ends, has peaks at St_e, St_L and $\mathrm{St}_L + \mathrm{St}_D$. Additionally, peaks of various power appear at harmonics between the cell shedding frequencies and half the dislocation frequency which did not appear for the cylinder with two free ends (see Figure 4.21 in the previous chapter). These frequencies do also appear in the cell transition region of the v spectra in Figure **??**, but it is unclear why this only appear in this case and not for the cylinder with two free ends.

The frequency spectrum for the fluctuating part of the drag force, shown in Figure 5.10, does also have very similar features to that of the cylinder with two free ends: It is dominated by a peak at the dislocation frequency with its subsequent harmonics and two lower peaks appearing at $2\mathrm{St}_e$ and $2\mathrm{St}_L$. Additionally, peaks occur at half the dislocation frequency and its harmonics as well.

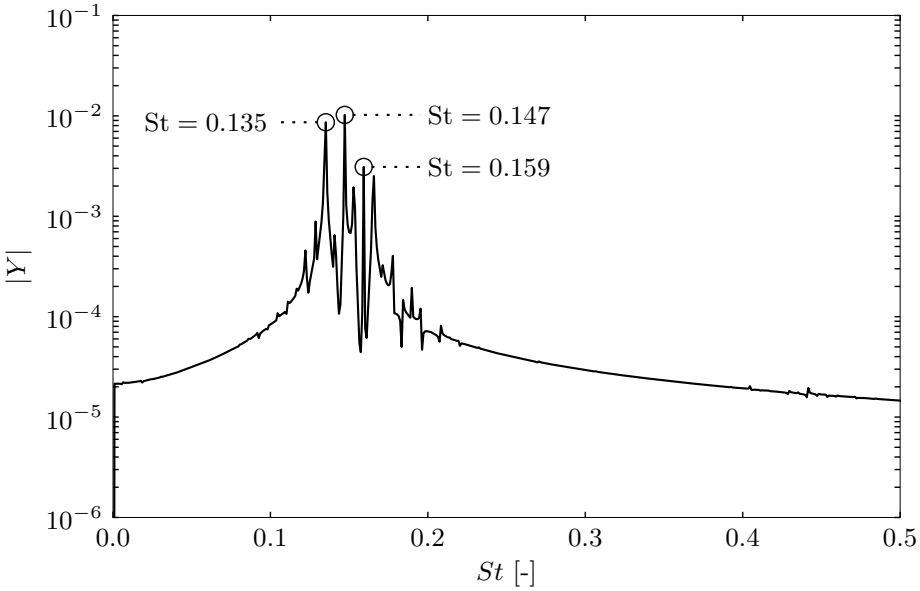

Figure 5.9: Frequency Spectrum of lift the force on a wall mounted cylinder with $^{L}/_{D} = 25$.

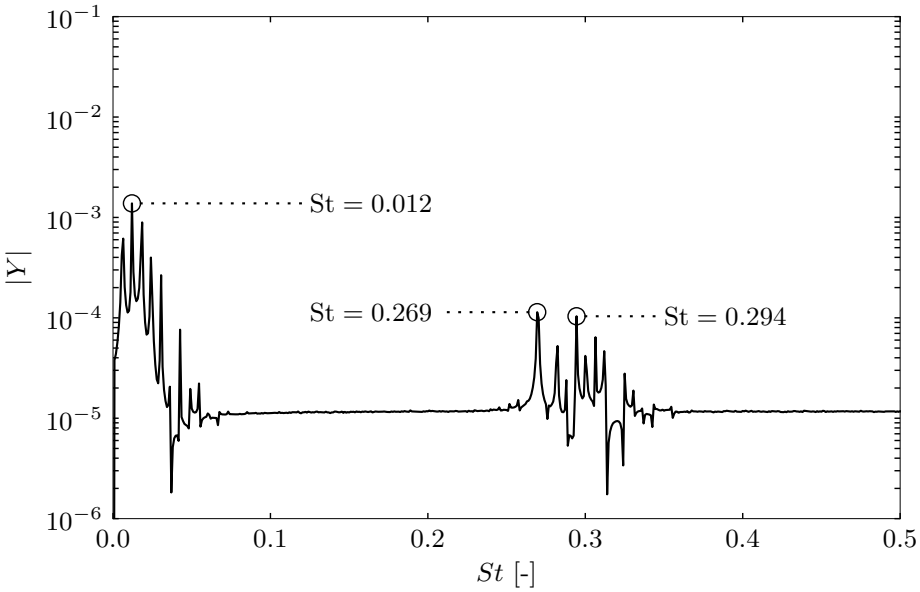

Figure 5.10: Frequency Spectrum of the fluctuating part of the drag force on a wall mounted cylinder with $^{L}/_{D} = 25$.

Chapter 6

Conclusions and Recommendations for Further Work

6.1 Conclusions

In the present study, the flow around finite cylinders at Re = 100 has been studied. The main goal of this study has been to isolate and investigate the flow features occurring behind the free end and the wall-cylinder junction. Two simulation cases were chosen, the first being a long ($^{L}/_{D} = 50$) cylinder with two free ends and the second being a wall mounted cylinder with $^{L}/_{D} = 25$. To reduce computation time, a symmetry condition was utilised at the spanwise centre of the cylinder with two free ends and $^{L}/_{D} = 50$.

Several authors have studied the flow around wall mounted cylinders (see e.g. Krajnoviä [16]) and studied the coherent flow structures in time averaged wake. The main flow features identified around a finite cylinder are the following:

Separation Bubble: At high Re, a separation bubble occurs above the free end. The present study shows that the flow remains attached over the free end at Re = 100.

Arch Vortex: Previous studies have identified an arch vortex forming behind the free end with arms extending downwards through the near wake of the cylinder. In the present study, this vortex was identified in the instantaneous as well as the mean flow. It was further found that in the instantaneous flow, the arms of the arch vortex follow the vortex shedding from below the free end.

Trailing Vortices: It has previously been shown that a pair of trailing vortices emerges behind the free end. These vortices have been identified in the mean flow. At Re = 100, their source has been found to be vortices shed from the cylinder which are bent horizontally near the free end.

Horseshoe Vortex System: At the wall-cylinder junction, other authors have identified a system of several vortices forming upstream and wrapping around the cylinder, both in laminar flow and in turbulent flow. In the present study a single horseshoe vortex were identified forming in front of the wall-cylinder junction, wrapping around the cylinder downstream.

The vortices behind long finite cylinders at Re = 100 are shed in two cells, one central cell and one smaller cell near each free end (Williamson [31]). Comparing the two simulated cases, it was found that the change in geometry did not affect the end cell vortex shedding frequency significantly. The central cell vortex shedding frequency, on the other hand, was reduced when the wall boundary condition was introduced and the aspect ratio was reduced. Comparing with data for an $^{L}/_{D} = 25$ cylinder with two free ends from Inoue and Sakuragi [11] it was found that the central cell vortex shedding frequency is influenced by both the introduction of a wall boundary condition and by the reduction of aspect ratio.

Investigating the vortex shedding in the wake of the cylinders it was shown that the vortices near the free end are bent horizontally through the $y = 0$ plane and connected to a vortex shed from the opposite side of the cylinder. Thus, vortices form a chain of vortex loops between the free ends. The same pattern of horizontally bent vortices connecting with their counterparts are also found near the wall boundary condition.

In the transition between the two cells, vortex dislocations occurs when the phase between the end cell vortex shedding and the central cell vortex shedding becomes large. Williamson [31] showed that this occurs with the beat frequency, i.e. the difference between the central cell and the end cell shedding frequencies, and this was confirmed in the present study. It was further shown that the dislocation frequency was present in a time signal of u in the wake at the spanwise centre of the cylinder with $^{L}/_{D} = 50$. Vortices near the wall boundary are not shed with a separate shedding frequency like the vortices near a free end and thus, no vortex dislocations occur near the wall boundary.

Comparing to the forces acting on a 2D cylinder, it was found that the lift force acting on the finite cylinders was reduced to approximately a tenth. This large reduction in lift force is due to the oblique vortex shedding causing cancelation effects on the global lift force. In contrast to the lift force, the reduction in drag compared to the 2D cylinder is found to be minor. The lift force was found to fluctuate with mainly three frequencies: One for each cell shedding frequency and a frequency which is one dislocation frequency larger than the central cell frequency.

A simple method, using a peak detection algorithm, for analysing large sets of time histories from measurement points in the wake has been outlined and tested. It

was found that the method detected the most important frequencies occurring in the measurements, but harmonics and low powered peaks of interest were often missed. The method proved to be a useful tool for getting an overview of the main flow features, but manual inspection of important regions are also necessary.

6.2 Recommendations for Further Work

Comparisons with other published results show that the results present here are similar to those obtained by other authors. There are however certain points where the quality of the simulations are questioned and further investigation could be appropriate:

Spatial and temporal refinements: The 2D grid convergence study in Section 3.2 shows that refining the grid and reducing the time step could affect the results. Additionally, the boundary layer in the case of the wall mounted cylinder is badly resolved. Refined simulations could be carried out to compare the vortex shedding frequencies and force coefficients found in the present study. At the same time, the grid spacing away from the cylinder and in the central region of the span could probably be relaxed.

Investigation of blockage above free end: There is some uncertainty whether the distance between the cylinder free end and the domain boundary is large enough not to affect the results. Figure 4.6 in Section 4.2 suggests that there is some blockage taking place, but its effect on the presented results is unknown.

The results of the present study shows promising insights into the basic flow features around finite cylinders. There are many opportunities for building upon these results, some possibilities are:

Spanwise distribution of lift and drag: The lift and drag forces analysed in the present study are the global forces acting on the cylinder. An investigation of how the different parts of the cylinder span contributes to the total force could reveal interesting details about the flow in the transitional region and the end cell. With the version of MGLET used in the present study it is not possible to obtain these results directly. A possible solution is to use the point measurement feature to measure the pressure at multiple points on the cylinder, but this will exclude the shear forces. Implementing this feature into MGLET would be a better, but probably a more difficult solution.

Increased Reynolds number: Many interesting phenomena occur during the transition to turbulence and in the turbulent wake of a cylinder and studying this with emphasis on the free end would be of interest. A particularly interesting case would be to determine when the separation bubble occurs above the free end and whether this influences the downwash and the trailing vortices.

Influence of free end geometry: As discussed briefly in Section 4.8, the free end could be shaped or fitted with a device that potentially modify the flow in an advantageous manner. Simulations of such such shapes and devices in various configurations could be and interesting extension to the currently published results on finite cylinders.

References

[1] C. J. Baker. "The laminar horseshoe vortex". *Journal of Fluid Mechanics* 95.02 (1979), pp. 347–367. DOI: 10.1017/S0022112079001506.

[2] C. J. Baker. "The turbulent horseshoe vortex". *Journal of Wind Engineering and Industrial Aerodynamics* 6.1-2 (1980), pp. 9–23. DOI: 10.1016/0167-6105(80)90018-5.

[3] C. J. Baker. "The position of points of maximum and minimum shear stress upstream of cylinders mounted normal to flat plates". *Journal of Wind Engineering and Industrial Aerodynamics* 18.3 (1985), pp. 263–274. DOI: 10.1016/0167-6105(85)90085-6.

[4] E. Billauer. *Peak detection using MATLAB*. 2009. URL: http://billauer.co.il/peakdet.html (visited on 04/12/2012).

[5] A. H. Day. *Theory and Practice of Marine CFD*. Lecture notes. University of Strathclyde. 2010.

[6] W. Dunn and S. Tavoularis. "Experimental studies of vortices shed from cylinders with a step-change in diameter". *Journal of Fluid Mechanics* 555 (2006), pp. 409–437. DOI: 10.1017/S002211200600927X.

[7] J. Fröhlich and W. Rodi. "LES of the flow around a circular cylinder of finite height". *International Journal of Heat and Fluid Flow* 25.3 (2004), pp. 537–548. DOI: 10.1016/j.ijheatfluidflow.2004.02.006.

[8] J. P. Gallardo Canabes. Personal communication, 14. May 2012.

[9] J. P. Gallardo Canabes. Personal communication, 5. June 2012.

[10] J. P. Gallardo Canabes. "Direct Numerical Simulation of the Flow Past a Curved Circular Cylinder". MA thesis. Norwegian University of Science and Technology, Department of Marine Technology, 2010.

[11] O. Inoue and A. Sakuragi. "Vortex shedding from a circular cylinder of finite length at low Reynolds numbers". *Physics of Fluids* 20.3 (2008), pp. 033601+. DOI: 10.1063/1.2844875.

[12] J. Jeong and F. Hussain. "On the identification of a vortex". *Journal of Fluid Mechanics* 285 (1995), pp. 69–94. DOI: 10.1017/S0022112095000462.

[13] T. A. Johnson and V. C. Patel. “Flow past a sphere up to a Reynolds number of 300”. *Journal of Fluid Mechanics* 378.02 (1999), pp. 19–70.

[14] T. Kambe. *Elementary fluid mechanics*. World Scientific, 2007. ISBN: 9812564160.

[15] T. Kawamura, M. Hiwada, T. Hibino, I. Mabuchi, and M. Kumada. “Flow around a Finite Circular Cylinder on a Flat Plate : Cylinder height greater than turbulent boundary layer thickness”. *Bulletin of JSME* 27.232 (1984), pp. 2142–2151.

[16] S. A. Krajnoviä. “Flow around a tall finite cylinder explored by large eddy simulation”. *Journal of Fluid Mechanics* 676 (2011), pp. 294–317. DOI: 10.1017/S0022112011000450.

[17] A. G. Kravchenko, P. Moin, and K. Shariff. “B-Spline Method and Zonal Grids for Simulations of Complex Turbulent Flows”. *Journal of Computational Physics* 151.2 (1999), pp. 757–789. DOI: 10.1006/jcph.1999.6217.

[18] Y. Liu, R. So, and Z. Cui. “A finite cantilevered cylinder in a cross-flow”. *Journal of Fluids and Structures* 20.4 (2005), pp. 589–609. DOI: 10.1016/j.jfluidstructs.2005.02.009.

[19] M. Manhart, F. Tremblay, and R. Friedrich. “MGLET: a parallel code for efficient DNS and LES of complex geometries”. *Parallel Computational Fluid Dynamics—Trends and Applications, Elsevier, Amsterdam* (2001), pp. 449–456.

[20] M. Manhart. “A zonal grid algorithm for DNS of turbulent boundary layers”. *Computers & Fluids* 33.3 (2004), pp. 435–461. DOI: 10.1016/S0045-7930(03)00061-6.

[21] G. Palau-Salvador, T. Stoesser, J. Fröhlich, M. Kappler, and W. Rodi. “Large Eddy Simulations and Experiments of Flow Around Finite-Height Cylinders”. *Flow, Turbulence and Combustion* 84.2 (2010), pp. 239–275. DOI: 10.1007/s10494-009-9232-0.

[22] C. W. Park and S. J. Lee. “Effects of free-end corner shape on flow structure around a finite cylinder”. *Journal of Fluids and Structures* 19.2 (2004), pp. 141–158. DOI: 10.1016/j.jfluidstructs.2003.12.001.

[23] R. J. Pattenden, S. R. Turnock, and X. Zhang. “Measurements of the flow over a low-aspect-ratio cylinder mounted on a ground plane”. *Experiments in Fluids* 39.1 (2005), pp. 10–21. DOI: 10.1007/s00348-005-0949-9.

[24] R. J. Pattenden, N. W. Bressloff, S. R. Turnock, and X. Zhang. “Unsteady simulations of the flow around a short surface-mounted cylinder”. *Int. J. Numer. Meth. Fluids* 53.6 (2007), pp. 895–914. DOI: 10.1002/fld.1309.

[25] N. Peller, A. L. Duc, F. Tremblay, and M. Manhart. “High-order stable interpolations for immersed boundary methods”. *Int. J. Numer. Meth. Fluids* 52.11 (2006), pp. 1175–1193. DOI: 10.1002/fld.1227.

[26] S. C. Roh and S. O. Park. "Vortical flow over the free end surface of a finite circular cylinder mounted on a flat plate". *Experiments in Fluids* 34.1 (2003), pp. 63–67. DOI: 10.1007/s00348-002-0532-6.

[27] R. L. Simpson. "Junction Flows". *Annual Review of Fluid Mechanics* 33.1 (2001), pp. 415–443. DOI: 10.1146/annurev.fluid.33.1.415.

[28] B. M. Sumer and J. Fredsøe. *Hydrodynamics Around Cylindrical Structures*. World Scientific Publishing Company. ISBN: 9810230567.

[29] F. M. White. *Fluid mechanics*. McGraw-Hill, 2008. ISBN: 9780071286459.

[30] Wikipedia. *Wingtip device — Wikipedia, The Free Encyclopedia*. [Online; accessed 8-June-2012]. 2012.

[31] C. H. K. Williamson. "Oblique and parallel modes of vortex shedding in the wake of a circular cylinder at low Reynolds numbers". *Journal of Fluid Mechanics* 206 (1989), pp. 579–627. DOI: 10.1017/S0022112089002429.

[32] J. H. Williamson. "Low-storage Runge-Kutta schemes". *Journal of Computational Physics* 35.1 (1980), pp. 48–56. DOI: 10.1016/0021-9991(80)90033-9.

[33] R. Winkelmann, J. Häuser, and R. D. Williams. "Strategies for parallel and numerical scalability of CFD codes". *Computer Methods in Applied Mechanics and Engineering* 174.3-4 (1999), pp. 433–456. DOI: 10.1016/S0045-7825(98)00308-9.

[34] M. M. Zdravkovich. *Flow Around Circular Cylinders Volume 2 Applications*. 1st. Oxford University Press, USA, 2002. ISBN: 0198565615.

Appendix

A.1 Overview of Electronic Appendix

The electronic appendix (found on the NTNU DAIM web pages), consists of the following folders:

animation-finite2free contains additional image sequences made from the data set of the finite cylinder with two free ends and $^{L}/_{D} = 50$.

bin contains various scripts used during the work, including scripts for extracting vector and scalar fields to VTK format. These scripts assumes the existence of the graph4 executable and the graph4old executable as `mglet_nolrz` and `mglet_nolrzOld` in the `PATH`.

inputFiles contains folders with input files and job scripts for the simulations presented in the present study. Some of the 2D simulation input files are unfortunately missing.